STABLE ASYMMETRIC SPIKE EQUILIBRIA FOR THE GIERER-MEINHARDT MODEL WITH A PRECURSOR FIELD

THEODORE KOLOKOLNIKOV *, FRÉDÉRIC PAQUIN-LEFEBVRE †, AND MICHAEL J. WARD ‡

Abstract. Precursor gradients in a reaction-diffusion system are spatially varying coefficients in the reaction-kinetics. Such gradients have been used in various applications, such as the head formation in the Hydra, to model the effect of pre-patterns and to localize patterns in various spatial regions. For the 1-D Gierer-Meinhardt (GM) model we show that a simple precursor gradient in the decay rate of the activator can lead to the existence of stable, asymmetric, two-spike patterns, corresponding to localized peaks in the activator of different heights. This is a qualitatively new phenomena for the GM model, in that asymmetric spike patterns are all unstable in the absence of the precursor field. Through a determination of the global bifurcation diagram of two-spike steady-state patterns, we show that asymmetric patterns emerge from a supercritical symmetry-breaking bifurcation along the symmetric two-spike branch as a parameter in the precursor field is varied. Through a combined analytical-numerical approach we analyze the spectrum of the linearization of the GM model around the two-spike steady-state to establish that portions of the asymmetric solution branches are linearly stable. In this linear stability analysis a new class of vector-valued nonlocal eigenvalue problem (NLEP) is derived and analyzed.

1. Introduction. We analyze the existence, linear stability, and bifurcation behavior of localized steady-state spike patterns for the Gierer-Meinhardt reaction-diffusion (RD) model in a 1-D domain where we have included a spatially variable coefficient for the decay rate of the activator. We will show that this spatial heterogeneity in the model, referred to as a precursor gradient, can lead to the existence of stable *asymmetric* two-spike equilibria, corresponding to steady-state spikes of different height (see the right panel of Fig. 2). This is a qualitatively new phenomenon for the GM model since, in the absence of a precursor field, asymmetric steady-state spike patterns for the GM model are always unstable [29]. A combination of analytical and numerical methods is used to determine parameter ranges where stable asymmetric steady-state patterns for the GM model with a simple precursor field can occur. We will show that these stable asymmetric equilibria emerge from a symmetry-breaking supercritical pitchfork bifurcation of symmetric spike equilibria as a parameter in the precursor field is varied.

Precursor gradients have been used in various specific applications of RD theory since the initial study by Gierer and Meinhardt in [8] for modeling head development in the Hydra. For other RD systems, precursor gradients have also been used in the numerical simulations of [11] to model the formation and localization of heart tissue in the Axolotl, which is a type of salamander. Further applications of such gradients for the GM model and other RD systems are discussed in [11], [12], [21], and [9]. With a precursor field, or with spatially variable diffusivities, the RD system does not generally admit a spatially uniform state. As a result, a conventional Turing stability approach is not applicable and the initial development of small amplitude patterns must be analyzed through either a slowly-varying assumption or from full numerical simulations (cf. [13], [22], [23], [20]).

In contrast to small amplitude patterns, in the singularly perturbed limit of a large diffusivity ratio $\mathcal{O}(\varepsilon^{-2}) \gg 1$, many two-component RD systems in 1-D admit

*Department of Mathematics and Statistics, Dalhouse University, Halifax, Canada. (corresponding author `tkolokol@gmail.com`)

†Department of Mathematics, UBC, Vancouver, Canada. (`paquinl@math.ubc.ca`)

‡Department of Mathematics, UBC, Vancouver, Canada. (`ward@math.ubc.ca`)

spike-type solutions. In this direction, there is a rather extensive analytical theory on the existence, linear stability and slow dynamics of spike-type solutions for many such RD systems in 1-D (see [5], [6], [14], [15], [24] [25], [26], and the references therein). To establish parameter regimes where spike-layer steady-states are linearly stable, one must analyze the spectrum of the operator associated with a linearization around the spike-layer solution. In this spectral analysis one must consider both the small eigenvalues of order $\mathcal{O}(\varepsilon^2)$ associated with near-translation invariance and the large $\mathcal{O}(1)$ eigenvalues that characterize any instabilities in the amplitudes of the spikes. These latter eigenvalues are associated with nonlocal eigenvalue problems (NLEPs), for which many rigorous results are available (cf. [4], [30], [28]).

Despite these advances, the effect of spatially heterogeneous coefficients in the reaction kinetics on spike existence, stability, and dynamics is much less well understood. With a precursor gradient, spike pinning can occur for the GM model (cf. [27], [31]) and for the Fitzhugh-Nagumo model (cf. [2], [10]), while a plant hormone (auxin) gradient is predicted to control the spatial locations of root formation in plant cells [1]. In other contexts, a spatial heterogeneity can trigger a self-replication loop consisting of spike formation, propagation, and annihilation against a domain boundary [19]. More recently, clusters of spikes that are confined as a result of a spatial heterogeneity have been analyzed in 1-D in [16] and [18] for the GM and Schnakenberg models, respectively, and in [17] for 2-D spot clusters of the GM model. In these recent approaches the RD system with clustered spikes is effectively approximated by a limiting equation for the spike density.

In our study we will consider the dimensionless GM model in 1-D with activator a and inhibitor h, and with a smooth precursor $\mu(x) > 0$ in the decay rate of the activator, given for $\varepsilon \ll 1$ by

$$a_t = \varepsilon^2 a_{xx} - \mu(x) a + \frac{a^2}{h}\,, \qquad |x| < L\,, \quad t > 0\,; \qquad a_x(\pm L, t) = 0\,, \tag{1.1a}$$

$$\tau h_t = h_{xx} - h + \varepsilon^{-1} a^2\,, \qquad |x| < L\,, \quad t > 0\,; \qquad h_x(\pm L, t) = 0\,. \tag{1.1b}$$

Although our analytical framework can be applied more generally, we will exhibit stable asymmetric spike-layer steady-states only for the specific precursor field

$$\mu(x) = 1 + bx^2\,, \tag{1.2}$$

where $b > 0$ is a bifurcation parameter. In our formulation in (1.1), we have for convenience fixed the inhibitor diffusivity at unity and will use the domain length L as the other bifurcation parameter.

In §2 we use a matched asymptotic approach to derive a differential algebraic system of ODEs (DAEs) for a collection of spikes for (1.1), under the assumption that the quasi-equilibrium spike pattern is stable on $\mathcal{O}(1)$ time-scales. The DAE system is written in terms of 1-D Green's functions, or equivalently as a tridiagonal system. In §3 we provide two alternative approaches for computing global branches of two-spike equilibria of the DAE system, for the μ as given in (1.2), and we formulate a generalized matrix eigenvalue problem characterizing the linear stability of branches of equilibria. Numerical results for steady-state spike locations and spike heights, denoting maxima of the inhibitor field, corresponding to global bifurcation branches of two-spike equilibria are shown in §3.2 in terms of the precursor parameter b and the domain half-length L. We show that the asymmetric branches of two-spike equilibria emerge from a symmetry breaking pitchfork bifurcation from the symmetric branch at a critical value $b = b_p(L)$. For $b > 0.076$, we show that this bifurcation is supercritical,

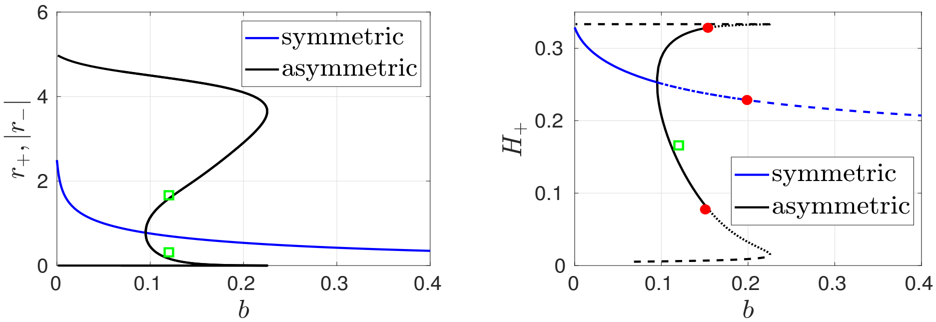

Fig. 1: Left: steady-state spike locations $x_1 = -r_-$ and $x_2 = r_+$ for $L = 5$ versus b in (1.2). Right: height H_+ of the rightmost spike versus b. Solid lines: linearly stable to both the small eigenvalues and the large (NLEP) eigenvalues when $\tau \ll 1$. Dash-dotted lines: unstable for the small eigenvalues but stable for the large eigenvalues when $\tau \ll 1$. Dashed line: stable to the small eigenvalues but unstable to the large eigenvalues when $\tau \ll 1$. Dotted line: unstable to both the small and large eigenvalues when $\tau \ll 1$. Red dots: zero-eigenvalue crossings for the NLEP. Green squares: the stable steady-state observed in the full PDE simulation of (1.1) shown in Fig. 2.

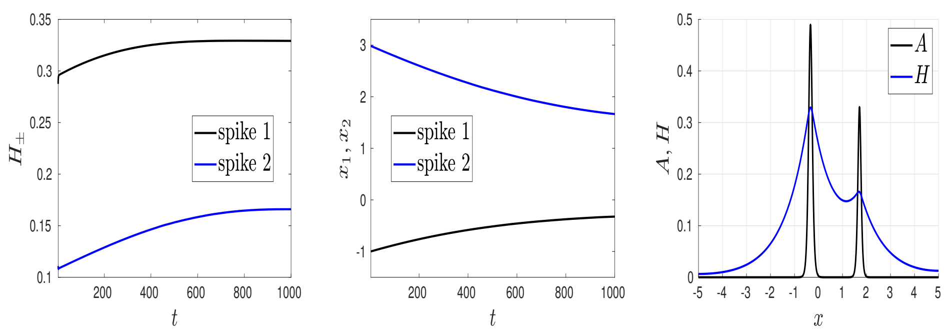

Fig. 2: Time-dependent PDE simulations of (1.1) with $L = 5$, $\varepsilon = 0.05$, and $\tau = 0.25$ for a precursor $\mu(x) = 1 + bx^2$ with $b = 0.12$. Initial condition is a quasi-equilibrium two-spike solution with spike locations $x_1(0) = -1$ and $x_2(0) = 3$. Spike heights (left panel), denoting maxima of the inhibitor field, and spike locations (middle panel) versus time. Right: the steady-state asymmetric two-spike equilibrium, stable to the small and large eigenvalues, corresponding to the green squares in Fig. 1.

and that the bifurcating branches of asymmetric equilibria are linearly stable as a steady-state solution of the DAE dynamics.

In §4 we derive a vector-valued NLEP characterizing spike amplitude instabilities of steady-state spike patterns of (1.1). For the case of symmetric two-spike equilibria, the vector-valued NLEP can be diagonalized, and we obtain necessary and sufficient conditions for the linear stability of these patterns when τ in (1.1) is sufficiently small. The resulting stability thresholds are shown in the global bifurcation plots in §3.2. However, for asymmetric two-spike equilibria, we obtain a new vector-valued NLEP that cannot be diagonalized, and for which the NLEP stability results in [30] are not directly applicable. For this new NLEP we determine analytically parameter values corresponding to zero-eigenvalue crossings, and for $\tau = 0$ we numerically compute any unstable eigenvalues by using a discretization of the vector-valued NLEP combined with a generalized matrix eigenvalue solver.

In 5 we confirm our global bifurcation and linear stability results through full PDE simulations of (1.1). As an illustration of our results, in Fig. 1 we plot the spike locations and spike heights corresponding to steady-state branches of symmetric and asymmetric two-spike equilibria in terms of the precursor parameter b for a domain half-length $L = 5$. The two branches of asymmetric two-spike equilibria result from an even reflection of solutions through the origin $x = 0$. In the right panel of Fig. 1, where we plot the spike heights, we show the linear stability properties for the small eigenvalues, as obtained from the linearization of the DAE system, and for the large eigenvalues, as determined from computations of the vector-valued NLEP. The time-dependent PDE simulations shown in Fig. 2 confirm that a quasi-equilibrium two-spike pattern tends to a stable asymmetric equilibrium on a long time scale. The paper concludes with a brief discussion in §6.

2. Derivation of the DAE System. We now derive a DAE system for the spike locations for an N-spike quasi-equilibrium pattern, which is valid in the absence of any $\mathcal{O}(1)$ time-scale instability of the pattern. Since this analysis is similar to that given in [15] with no precursor field and in [27] for a precursor field, but with only one spike, we only briefly outline the analysis here.

The spike locations x_j, for $j = 1, \ldots, N$, are assumed to satisfy $|x_{j+1} - x_j| \gg \mathcal{O}(\varepsilon)$, with $|x_1 + L| \gg \mathcal{O}(\varepsilon)$ and $|L - x_N| \gg \mathcal{O}(\varepsilon)$. As shown in [15] and [27], in the absence of any $\mathcal{O}(1)$ time-scale instability of the spike amplitudes, the spikes will evolve on the long time-scale $\sigma = \varepsilon^2 t$, and so we write $x_j = x_j(\sigma)$.

To derive a DAE system for $x_j(\sigma)$, for $j = 1, \ldots, N$, we first construct the solution in the inner region near the j-th spike. We introduce the inner expansion

$$a = A_0 + \varepsilon A_1 + \ldots\,, \qquad h = H_0 + \varepsilon H_1 + \cdots\,, \tag{2.1}$$

where $A_i = A_i(y, \sigma)$ and $H_i = H_i(y, \sigma)$ for $i = 0, 1$ and $y = \varepsilon^{-1}(x - x_j)$. Upon substituting (2.1) into (1.1), and using $a_t = -\varepsilon x_j' A_{0y} + \mathcal{O}(\varepsilon^2)$ where $x_j' \equiv dx_j/d\sigma$, we collect powers of ε to obtain the following leading-order problem on $-\infty < y < \infty$:

$$A_{0yy} - \mu_j A_0 + A_0^2/H_0 = 0\,, \qquad H_{0yy} = 0\,, \tag{2.2}$$

where $\mu_j \equiv \mu(x_j)$. At next order, we conclude on $-\infty < y < \infty$ that

$$\mathcal{L} A_1 \equiv A_{1yy} - \mu_j A_1 + \frac{2A_0}{H_0} A_1 = \frac{A_0^2}{H_0^2} H_1 + y\mu'(x_j) A_0 - x_j' A_{0y}\,, \tag{2.3a}$$

$$H_{1yy} = -A_0^2\,. \tag{2.3b}$$

From (2.2) we get that $H_0 = H_{0j}(\sigma)$, where H_{0j}, independent of y, is to be determined. In addition, the spike profile is given by

$$A_0 = \mu_j H_{0j} w\left(\sqrt{\mu_j} y\right) \qquad \text{where} \qquad w(z) = \frac{3}{2}\,\mathrm{sech}^2(z/2)\,, \tag{2.4}$$

where $w(0) > 0$ with $w'(0) = 0$, is the well-known homoclinic solution to

$$w'' - w + w^2 = 0\,, \quad -\infty < z < \infty\,, \quad w \to 0 \quad \text{as} \quad |z| \to \infty\,. \tag{2.5}$$

Since $\mathcal{L}A_{0y} = 0$, the solvability condition for (2.3a) is that

$$x_j' \int A_{0y}^2 \, dy = \mu'(x_j) \int y A_0 A_{0y} \, dy + \int \frac{A_0^2}{H_{0j}^2} H_1 A_{0y} \, dy$$
$$= \frac{\mu'(x_j)}{2} \int y \left(A_0^2\right)_y \, dy + \frac{1}{3H_{0j}^2} \int \left(A_0^3\right)_y H_1 \, dy \tag{2.6}$$
$$= -\frac{\mu'(x_j)}{2} \int A_0^2 \, dy - \frac{1}{3H_{0j}^2} \int A_0^3 H_{1y} \, dy \,,$$

where we have used integration by parts and the shorthand notation $\int = \int_{-\infty}^{\infty}$. From a further integration by parts on the last term on the last line in (2.6), and using the fact that $H_{1yy} = -A_0^2$ is even, we obtain that

$$x_j' = -\frac{\mu'(x_j)}{2} I_1 - \frac{1}{6H_{0j}^2} I_2 \left(\lim_{y \to +\infty} H_{1y} + \lim_{y \to -\infty} H_{1y} \right) , \tag{2.7}$$

in terms of the integral ratios I_1 and I_2 defined by

$$I_1 \equiv \frac{\int A_0^2 \, dy}{\int A_{0y}^2 \, dy} \,, \qquad I_2 \equiv \frac{\int A_0^3 \, dy}{\int A_{0y}^2 \, dy} \,. \tag{2.8}$$

By multiplying the ODE for A_0 in (2.2) first by A_{0y} and then by A_0, we integrate the two resulting expressions to obtain an algebraic system for I_1 and I_2, which yields

$$I_1 = \frac{5}{\mu_j} \,, \qquad I_2 = 6H_{0j} \,. \tag{2.9}$$

Upon using (2.9) in (2.7), we conclude for each $j = 1, \ldots, N$ that

$$x_j' = -\frac{5}{2} \frac{\mu'(x_j)}{\mu(x_j)} - \frac{1}{H_{0j}} \left(\lim_{y \to +\infty} H_{1y} + \lim_{y \to -\infty} H_{1y} \right) . \tag{2.10}$$

To determine H_{0j} for $j = 1, \ldots, N$ and the remaining term in (2.10) we need to determine the outer solution.

Now in the outer region, defined away from $\mathcal{O}(\varepsilon)$ regions near each x_j, a is exponentially small. In the sense of distributions we then use $A_0 = H_{0j}\mu_j w(\sqrt{\mu_j} y)$ to calculate across each $x = x_j$ that

$$\frac{1}{\varepsilon} a^2 \to \left(\int A_0^2 \, dy \right) \delta(x - x_j) = \mu_j^{3/2} H_{0j}^2 \left(\int w^2(z) \, dz \right) \delta(x - x_j) = 6\mu_j^{3/2} H_{0j}^2 \delta(x - x_j) \,, \tag{2.11}$$

owing to the fact that $\int w^2 \, z = \int w \, dz = 6$. In this way, the outer problem for h is

$$h_{xx} - h = -6 \sum_{j=1}^{N} H_{0j}^2 \mu_j^{3/2} \delta(x - x_j) \,, \quad |x| \leq L \,; \qquad h_x(\pm L, \sigma) = 0 \,. \tag{2.12}$$

The solution to (2.12) is

$$h(x) = \sum_{i=1}^{N} H_{0i}^2 \mu_i^{3/2} G(x; x_i) \,, \tag{2.13}$$

where $G(x;x_i)$ is the 1-D Green's function satisfying

$$G_{xx} - G = -\delta(x-x_i)\,, \quad |x| \le L\,; \qquad G_x(\pm L; x_i) = 0\,. \tag{2.14}$$

To match with the inner solutions near each x_j, we require for each $j = 1,..,N$ that

$$h(x_j) = H_{0j}\,, \qquad \lim_{y\to\infty} H_{1y} + \lim_{y\to -\infty} H_{1y} = h_x(x_{j+}) + h_x(x_{j-})\,. \tag{2.15}$$

In this way, by using (2.15) in (2.13) and (2.10) we obtain the following DAE system for slow spike motion:

$$\frac{dx_j}{d\sigma} = -\frac{5}{2}\frac{\mu'(x_j)}{\mu_j} - \frac{12}{H_j}\left(\mu_j^{3/2} H_j^2 \langle G_x\rangle_j + \sum_{\substack{i=1\\ i\neq j}}^{N} \mu_i^{3/2} H_i^2 G_x(x_j;x_i)\right)\,, \tag{2.16a}$$

$$H_j = 6\sum_{i=1}^{N} \mu_i^{3/2} H_i^2 G(x_j;x_i)\,, \tag{2.16b}$$

where $\mu_j \equiv \mu(x_j)$, $\langle G_x\rangle_j \equiv \left[G_x(x_{j+};x_i) + G_x(x_{j-};x_i)\right]/2$, and $G(x;x_j)$ is the Green's function satisfying (2.14). In (2.16), we have relabeled H_{0j} by H_j.

A simple special case of (2.16) is for the infinite-line problem with $L\to\infty$, for which $G(x;x_i) = \frac{1}{2}e^{-|x-x_i|}$. For this case, we calculate $\langle G_x\rangle_j = 0$ and $G_x(x_j;x_i) = -\frac{1}{2}\text{sign}(x_j - x_i)e^{-|x_j-x_i|}$. In this way, we can rewrite (2.16) as

$$\frac{dx_j}{d\sigma} = -\frac{5}{2}\frac{\mu'(x_j)}{\mu_j} + \frac{1}{H_j}\sum_{\substack{i=1\\ i\neq j}}^{N} S_i\,\text{sign}(x_j - x_i)e^{-|x_j-x_i|}\,, \tag{2.17a}$$

$$H_j = \frac{1}{2}\sum_{i=1}^{N} S_i e^{-|x_j-x_i|}\,, \qquad H_j = \left(\frac{S_j}{6\mu_j^{3/2}}\right)^{1/2}\,. \tag{2.17b}$$

From (2.16a), we observe that the DAE dynamics for the j-th spike is globally coupled to all of the other spikes through full matrices. We now proceed as in [15] to derive an equivalent representation of (2.16a) that is based only on nearest neighbor interactions. To do so, we first write (2.16) compactly in matrix form as

$$\frac{d\boldsymbol{x}}{d\sigma} = -\frac{5}{2}\boldsymbol{\mu_p} - 2\mathcal{H}^{-1}\mathcal{P}\mathcal{G}^{-1}\boldsymbol{h}\,, \qquad \mathcal{G}^{-1}\boldsymbol{h} = 6\,\mathcal{U}\boldsymbol{h}^2\,, \tag{2.18}$$

where $\mathcal{G}$ and $\mathcal{P}$ are defined in terms of the Green's function by

$$\mathcal{G} \equiv \begin{pmatrix} G(x_1;x_1) & \cdots & G(x_1;x_N)\\ \vdots & \ddots & \vdots \\ G(x_N;x_1) & \cdots & G(x_N;x_N)\end{pmatrix}\,,\ \mathcal{P} \equiv \begin{pmatrix} \langle G_x\rangle_1 & \cdots & G_x(x_1;x_N)\\ \vdots & \ddots & \vdots \\ G_x(x_N;x_1) & \cdots & \langle G_x\rangle_N\end{pmatrix}\,. \tag{2.19a}$$

In (2.18), $\mathcal{U}$ and $\mathcal{H}$ are diagonal matrices with diagonal entries $(\mathcal{U})_{jj} = \mu(x_j)$ and $(\mathcal{H})_{jj} = H_j$ for $j = 1,\ldots,N$, and we have defined

$$\boldsymbol{h} \equiv \begin{pmatrix} H_1\\ \vdots\\ H_N\end{pmatrix}\,, \qquad \boldsymbol{h}^2 \equiv \begin{pmatrix} H_1^2\\ \vdots\\ H_N^2\end{pmatrix}\,, \qquad \boldsymbol{\mu_p} \equiv \begin{pmatrix} \frac{\mu'(x_1)}{\mu(x_1)}\\ \vdots\\ \frac{\mu'(x_N)}{\mu(x_N)}\end{pmatrix}\,. \tag{2.19b}$$

As shown in Appendix A of [15] (see also Appendix A of [14]), the inverse $\mathcal{B} \equiv \mathcal{G}^{-1}$ of the Green's matrix and the product $\mathcal{P}\mathcal{G}^{-1}$ are each triangular matrices of the form

(2.20a)
$$\mathcal{B} = \begin{pmatrix} c_1 & d_1 & & 0 \\ d_1 & \ddots & \ddots & \\ & \ddots & \ddots & d_{N-1} \\ 0 & & d_{N-1} & c_N \end{pmatrix}, \quad 2\mathcal{P}\mathcal{B} \equiv \mathcal{A} = \begin{pmatrix} e_1 & -d_1 & & 0 \\ d_1 & \ddots & \ddots & \\ & \ddots & \ddots & -d_{N-1} \\ 0 & & d_{N-1} & e_N \end{pmatrix},$$

where the matrix entries are given by

(2.20b)
$$\begin{aligned} &c_1 = \coth(x_2 - x_1) + \tanh(L + x_1)\,, \quad c_N = \coth(x_N - x_{N-1}) + \tanh(L - x_N)\,, \\ &c_j = \coth(x_{j+1} - x_j) + \coth(x_j - x_{j-1})\,, \quad j = 2, \ldots N-1\,, \\ &e_1 = \tanh(L + x_1) - \coth(x_2 - x_1)\,, \quad e_N = \coth(x_N - x_{N-1}) - \tanh(L - x_N)\,, \\ &e_j = \coth(x_j - x_{j-1}) - \coth(x_{j+1} - x_{j-1})\,, \quad j = 2, \ldots N-1\,, \\ &d_j = -\operatorname{csch}(x_{j+1} - x_j)\,, \quad j = 1, \ldots, N-1\,. \end{aligned}$$

For the infinite-line problem, we calculate for the limit $L \to \infty$ that

$$\begin{aligned} &c_1 \to \frac{2}{1 - e^{-2(x_2 - x_1)}}\,, \quad c_N \to \frac{2}{1 - e^{-2(x_N - x_{N-1})}}\,, \quad \text{as} \quad L \to \infty\,, \\ &e_1 \to \frac{2}{1 - e^{2(x_2 - x_1)}}\,, \quad e_N \to -\frac{2}{1 - e^{2(x_N - x_{N-1})}}\,, \quad \text{as} \quad L \to \infty\,. \end{aligned} \tag{2.21}$$

Finally, upon substituting (2.20) into (2.18), we obtain the following more tractable, but equivalent, tridiagonal representation of the DAE dynamics (2.16):

$$\frac{d\boldsymbol{x}}{d\sigma} = -\frac{5}{2}\boldsymbol{\mu_p} - \mathcal{H}^{-1}\mathcal{A}\boldsymbol{h}\,, \qquad \mathcal{B}\boldsymbol{h} = 6\,\mathcal{U}\boldsymbol{h}^2\,. \tag{2.22}$$

3. Global Bifurcation Diagram of Spike Equilibria.

In this section we analyze bifurcation behavior for two-spike equilibria of (2.22) and study their stability properties in terms of equilibrium points of the DAE system (2.22). From (2.22), the equilibria satisfy the nonlinear algebraic system $\mathcal{F}(x_1, x_2, H_1, H_2) = \mathbf{0}$ for $\mathcal{F} \in \mathbb{R}^4$, given component-wise by

(3.1)
$$\begin{aligned} &\mathcal{F}_1 \equiv -\frac{5}{2}\frac{\mu'(x_1)}{\mu(x_1)} - e_1 + d_1\frac{H_2}{H_1}\,, \qquad \mathcal{F}_2 \equiv -\frac{5}{2}\frac{\mu'(x_2)}{\mu(x_2)} - e_2 - d_1\frac{H_1}{H_2}\,, \\ &\mathcal{F}_3 = 6\left[\mu(x_1)\right]^{3/2} H_1^2 - c_1 H_1 - d_1 H_2\,, \qquad \mathcal{F}_4 = 6\left[\mu(x_2)\right]^{3/2} H_2^2 - d_1 H_1 - c_2 H_2\,. \end{aligned}$$

The linear stability properties of an equilibrium state (r_+, r_-, H_+, H_-) of the DAE dynamics (2.22) is based on the eigenvalues ω of the matrix eigenvalue problem

$$J\boldsymbol{v} = \omega\mathcal{D}\boldsymbol{v}\,, \tag{3.2}$$

where $J \equiv D\mathcal{F}$ is the Jacobian of $\mathcal{F}$ and $\mathcal{D}$ is the rank-defective diagonal matrix with matrix entries $(\mathcal{D})_{11} = 1$, $(\mathcal{D})_{22} = 1$, $(\mathcal{D})_{33} = 0$, and $(\mathcal{D})_{44} = 0$. Since $\operatorname{rank}(\mathcal{D}) = 2$, (3.2) has two infinite eigenvalues. The signs of the real parts of the remaining two matrix eigenvalues classify the linear stability of the equilibrium point for (2.22).

We will refer to these eigenvalues as the "small eigenvalues" for spike stability in accordance with the term used in [14] in the absence of a precursor field.

We now outline a simple approach for computing branches of solutions to $\mathcal{F} = \mathbf{0}$ in terms of a parameter in the precursor field $\mu(x)$. An alternative formulation is given in §3.1 below. For the first approach, we introduce the spike height ratio s by

$$s \equiv \frac{H_2}{H_1}\,, \tag{3.3}$$

and reduce (3.1) to the three-component system $\mathcal{N}(x_1, x_2, s) = 0$ with $\mathcal{N} \in \mathbb{R}^3$ defined by

$$\mathcal{N}_1 \equiv -\frac{5}{2}\frac{\mu'(x_1)}{\mu(x_1)} - e_1 + d_1 s\,, \qquad \mathcal{N}_2 \equiv -\frac{5}{2}\frac{\mu'(x_2)}{\mu(x_2)} - e_2 - \frac{d_1}{s}\,, \tag{3.4a}$$

$$\mathcal{N}_3 = s^2\left[\mu(x_2)\right]^{3/2}(c_1 + d_1 s) - \left[\mu(x_1)\right]^{3/2}(d_1 + c_2 s)\,. \tag{3.4b}$$

In terms of solutions to $\mathcal{N}_j = 0$ for $j = 1, \ldots, 3$ the spike heights are

$$H_1 = \frac{(c_1 + d_1 s)}{6\left[\mu(x_1)\right]^{3/2}}\,, \qquad H_2 = sH_1\,. \tag{3.4c}$$

In (3.4) and (3.1), the constants c_1, c_2, d_1, e_1, and e_2 are defined by (see (2.20b)):

$$\begin{aligned} &c_1 = \coth(x_2 - x_1) + \tanh(L + x_1)\,, \quad c_2 = \coth(x_2 - x_1) + \tanh(L - x_2)\,,\\ &e_1 = \tanh(L + x_1) - \coth(x_2 - x_1)\,, \quad e_2 = \coth(x_2 - x_1) - \tanh(L - x_2)\,,\\ &d_1 = -\operatorname{csch}(x_2 - x_1)\,. \end{aligned} \tag{3.5}$$

For the special case where $\mu(x)$ is even, i.e. $\mu(x) = \mu(-x)$, we label "symmetric" spike equilibria as those solutions of (3.4) for which $s = 1$ and $x_2 = -x_1$. For this case, $c_1 = c_2$, $e_2 = -e_1$, and $\mathcal{N}_3(-x_2, x_2, 1) = 0$. Moreover, we calculate that $e_2 + d_1 = \tanh(x_2) - \tanh(L - x_2)$, and so (3.4) reduces to finding a root x_2 on $0 < x_2 < L$ to the scalar equation $\mathcal{S}(x_2) = 0$ given by

$$\mathcal{S}(x_2) \equiv \frac{\mu'(x_2)}{\mu(x_2)} - \frac{2}{5}\left[\tanh(L - x_2) - \tanh(x_2)\right]\,. \tag{3.6}$$

It readily follows that when $\mu(x) > 0$ and $\mu'(x) > 0$, there is always a root to $\mathcal{S} = 0$ with $0 < x_2 < L/2$. Our bifurcation results shown below are for the quadratic precursor field $\mu(x) = 1 + bx^2$ with $b \geq 0$, as given in (1.2). For this special choice of μ, instead of computing $x_2 = x_2(b)$ in (3.6) using Newton iterations, we can solve $\mathcal{S} = 0$ in (3.6) in the explicit form $b = b(x_2)$, where

$$b = \frac{\left[\tanh(L - x_2) - \tanh(x_2)\right]}{x_2\left(5 - x_2\left[\tanh(L - x_2) - \tanh(x_2)\right]\right)}\,. \tag{3.7}$$

By varying x_2 on $0 < x_2 < L/2$ in (3.7), and keeping only points where $b > 0$, we obtain a simple parametric representation of the symmetric two-spike equilibrium solution branch with $x_1 = -x_2$. The common spike heights are given by

$$H_c \equiv H_{1,2} = \frac{1}{6\left[\mu(x_2)\right]^{3/2}}\left[\tanh(x_2) + \tanh(L - x_2)\right]\,. \tag{3.8}$$

The linear stability with respect to the DAE dynamics (2.22) at each value of b on this symmetric solution branch is obtained from a numerical computation of the matrix spectrum of the generalized eigenvalue problem (3.2).

To parameterize asymmetric two-spike equilibria for the special case $\mu = 1 + bx^2$, we isolate b from setting $\mathcal{N}_1 = \mathcal{N}_2 = 0$ in (3.4a). By equating the resulting two expressions for b, we obtain an equation relating x_1 and x_2, in which we treat s as a parameter. The remaining equation is $\mathcal{N}_3 = 0$ from (3.4b). In this way, for $s \neq 1$, we calculate solutions $x_1 = x_1(s)$, $x_2 = x_2(s)$ to the two-component coupled system

$$\begin{gathered}\left(x_2^2 - x_1^2\right)(e_1 - d_1 s)\left(e_2 + \frac{d_1}{s}\right) - 5\left[x_2 (e_1 - d_1 s) - x_1\left(e_2 + \frac{d_1}{s}\right)\right] = 0\,, \\ s^2 \left[\mu(x_2)\right]^{3/2}(c_1 + d_1 s) - \left[\mu(x_1)\right]^{3/2}(d_1 + c_2 s) = 0\,,\end{gathered} \tag{3.9a}$$

in which $\mu(x) = 1 + bx^2$, where b is given by

$$b = \frac{d_1 s - e_1}{5x_1 + x_1^2(e_1 - d_1 s)}\,. \tag{3.9b}$$

The spike heights are then obtained from (3.4c) in terms of the parameter s. This reformulation of (3.4) gives a convenient approach for parameterizing solution branches of asymmetric two-spike equilibria in terms of the spike height ratio s. For the finite domain case $L < \infty$, the coefficients c_1, c_2, e_1, e_2, and d_1, are given in (3.5), while when $L = \infty$, we use $c_1 = c_2 = 2/(1 - e^{-2(x_2 - x_1)})$ and $e_1 = -e_2 = \frac{2}{1 - e^{2(x_2 - x_1)}}$. Finally, at each point on these solution branches the spectrum of the generalized eigenvalue problem (3.2) is computed to determine the linear stability of asymmetric spike equilibria to the small eigenvalues.

Although this approach works well for moderate values of s, for either very large or small values of s the nonlinear algebraic system (3.9) is rather poorly conditioned. As a result we need an alternative approach to compute two-spike equilibria.

3.1. Two-Spike Equilibria: An Alternative Parameterization. An alternative approach to parameterize symmetric and asymmetric two-spike equilibrium solution branches for the special case where $\mu(x)$ is even is described in Appendix A. This approach leads to a nonlinear algebraic system in terms of r_+, r_-, and ℓ, where ℓ is the symmetry point in the interval $-r_- < \ell < r_+$ at which $h_x = 0$. Here $x_2 = r_+$ and $x_1 = -r_-$ are the two steady-state spike locations with spike heights $H_\pm$. As shown in Appendix A, with this formulation we must solve

$$f(r_+, \ell) = 0\,, \qquad f(r_-, -\ell) = 0\,, \qquad \xi(r_+, \ell) - \xi(r_-, -\ell) = 0\,, \tag{3.10a}$$

for $r_\pm$ and ℓ, where $f(r, \ell)$ and $\xi(r, \ell)$ are defined by

$$f(r, \ell) = \frac{\mu'(r)}{\mu(r)} + \frac{4}{5}\frac{\langle g_x(r, r; \ell)\rangle}{g(r, r; \ell)}\,, \qquad \xi(r, \ell) = \frac{\mu^{-3/2}(r)}{6}\frac{g(\ell, r; \ell)}{g^2(r, r; \ell)}\,, \tag{3.10b}$$

where $\langle g_x(r, r; \ell)\rangle$ indicates the average of g_x across $x = r$. Here $g(x, r; \ell)$ is the 1-D Green's function, with Dirac point r and left domain endpoint ℓ, satisfying

$$g_{xx} - g = -\delta(x - r)\,, \quad \ell < x < L\,; \qquad g_x = 0 \quad \text{at} \quad x = \ell\,,\, L\,. \tag{3.11}$$

In the infinite domain case, where $L = \infty$, we calculate that

$$g(r, r; \ell) = \frac{1}{2}\left(1 + e^{2(\ell - r)}\right)\,, \quad g(\ell, r; \ell) = e^{\ell - r}\,, \quad \langle g_x(r, r; \ell)\rangle = -\frac{1}{2}e^{2(\ell - r)}\,, \tag{3.12}$$

so that (3.10b) becomes

$$f(r,\ell) = \frac{2br}{1+br^2} - \frac{4}{5\left(1+e^{2(r-\ell)}\right)}\,, \quad \xi(r,\ell) = \frac{2(1+br^2)^{-3/2}}{3}\frac{e^{\ell-r}}{(1+e^{2(\ell-r)})^2}\,. \tag{3.13}$$

The spike heights for the inhibitor are defined in terms of $r_\pm$ by

$$H_\pm = \frac{\mu^{-3/2}(r_\pm)}{6g(r_\pm, r_\pm; \pm\ell)} = \frac{(1+br_\pm^2)^{-3/2}}{3(1+e^{2(\pm\ell - r_\pm)})}\,. \tag{3.14}$$

Alternatively, for the finite domain case, we calculate from (3.11) that

$$\begin{gathered} g(r,r;\ell) = \frac{\cosh(r-\ell)\cosh(r-L)}{\sinh(L-\ell)}\,, \quad g(\ell,r;\ell) = \frac{\cosh(r-L)}{\sinh(L-\ell)}\,, \\ \langle g_x(r,r;\ell)\rangle = \frac{\sinh(2r-L-\ell)}{2\sinh(L-\ell)}\,, \end{gathered} \tag{3.15}$$

so that (3.10b) becomes

$$f(r,\ell) = \frac{2br}{1+br^2} + \frac{2\sinh(2r-L-\ell)}{5\cosh(r-\ell)\cosh(r-L)}\,, \quad \xi(r,\ell) = \frac{(1+br^2)^{-3/2}\sinh(L-\ell)}{6\cosh^2(r-\ell)\cosh(r-L)}\,. \tag{3.16}$$

For this finite domain case, the spike heights are given by

$$H_\pm = -\frac{(1+br_\pm^2)^{-3/2}\sinh(\pm\ell - L)}{6\cosh(\pm\ell - r_\pm)\cosh(r_\pm - L)}\,. \tag{3.17}$$

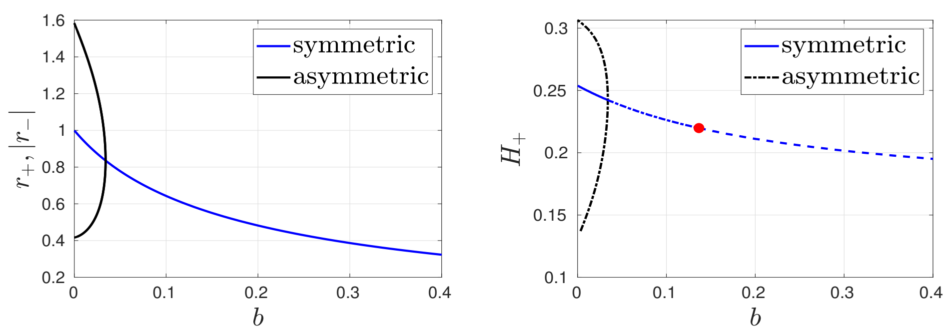

Fig. 3: Left: steady-state spike locations r_+ and $-r_-$ for $L = 2$ versus b in (1.2). Right: height H_+ of the rightmost spike versus b. Solid lines: linearly stable to both the small eigenvalues and the large (NLEP) eigenvalues when $\tau \ll 1$. Dash-dotted lines: unstable for the small eigenvalues but stable for the large eigenvalues when $\tau \ll 1$. Dashed line: stable to the small eigenvalues but unstable to the large eigenvalues when $\tau \ll 1$. Red dot: zero-eigenvalue crossing of the NLEP on the symmetric branch. Bifurcation from symmetric to asymmetric equilibria is subcritical.

To compute branches of two-spike equilibria as either b or L is varied, we write (3.10) for $r_\pm$ and ℓ in the form $\boldsymbol{F}(\mathbf{u},\zeta) = 0$, where

$$\boldsymbol{F}(\mathbf{u},\zeta) \equiv \begin{pmatrix} f(r_+, l) \\ f(r_-, -l) \\ \xi(r_+, l) - \xi(r_-, -l) \end{pmatrix}\,, \quad \text{with} \quad \mathbf{u} \equiv (r_+, r_-, l)^T\,, \quad \zeta \equiv (b, L)^T\,. \tag{3.18}$$

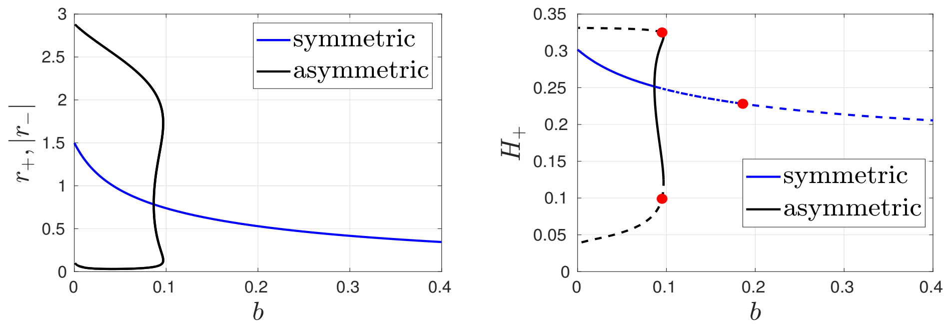

Fig. 4: Similar caption as in Figs. 1 and 3. Left: steady-state spike locations r_+ and $-r_-$ for $L = 3$ versus b. The pitchfork bifurcation is now supercritical. Right: height H_+ of the rightmost spike versus b. Solid lines: linearly stable to both the small eigenvalues and the large (NLEP) eigenvalues when $\tau \ll 1$. Dash-dotted lines: unstable for the small eigenvalues but stable for the large eigenvalues when $\tau \ll 1$. Dashed line: stable to the small eigenvalues but unstable to the large eigenvalues when $\tau \ll 1$. There are only very small (nearly indistinguishable) zones along the asymmetric branches that are unstable to the small eigenvalues. Red dots are where the NLEP has a zero-eigenvalue crossing.

Families of solutions and branch points (corresponding to symmetry-breaking pitchfork bifurcations) of this nonlinear system were computed using the two software packages AUTO (cf. [7]) and COCO (cf. [3]), thereby validating the diagrams provided in Figs. 1, 3, 4, 5, 6 and 7. In Appendix A we give explicit formulas for the Jacobian of $\boldsymbol{F}$ with respect to $\mathbf{u}$ and the parameter vector ζ, since providing analytical Jacobians significantly improves the performance and accuracy of continuation routines as opposed to using numerical Jacobians based on centered differences.

3.2. Numerical Bifurcation Results for Two-Spike Equilibria. For $L = 2$, in the left panel of Fig. 3 we plot the numerically computed steady-state spike locations versus the precursor parameter b. In the right panel of Fig. 3, we plot the corresponding height H_+ of the rightmost steady-state spike versus b. In addition, in our plot of H_+ versus b we indicate by various line shadings the linear stability properties of the steady-state solutions. We first observe that asymmetric two-spike equilibria emerge from a subcritical symmetry-breaking bifurcation from the branch of symmetric two-spike equilibria at the critical value $b \approx 0.034$. However, the asymmetric solution branches are all unstable with regards to the small eigenvalues, as indicated by the dash-dotted black curves in the right panel of Fig. 3. Below in the left panel of Fig. 9 we show from a numerical computation of a vector-valued NLEP that these asymmetric branches are all stable on an $\mathcal{O}(1)$ time-scale when τ is sufficiently small. These linear stability properties are qualitatively similar to that for two-spike equilibria of the GM model with no precursor field (cf. [29]).

In the left and right panels of Fig. 4 and Fig. 1 we plot similar global bifurcation results for two-spike equilibria when $L = 3$ and $L = 5$, respectively. For these values of L, we observe that the symmetry-breaking bifurcation is now supercritical and that a large portion of the bifurcating asymmetric two-spike branch of equilibria is linearly stable with regards to the small eigenvalues. Moreover, as shown below in the middle

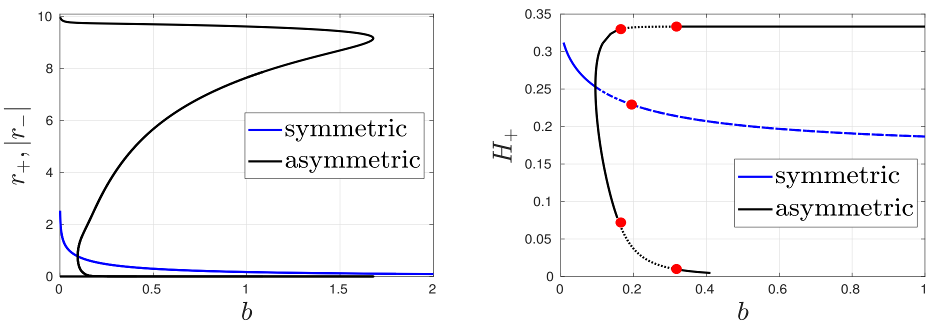

Fig. 5: Left: steady-state spike locations r_+ and $-r_-$ for $L = 10$ versus b. Right: height H_+ of the rightmost spike versus b. Solid lines: linearly stable to both the small eigenvalues and the large (NLEP) eigenvalues when $\tau \ll 1$. Dash-dotted lines: unstable for the small eigenvalues but stable for the large eigenvalues when $\tau \ll 1$. Dashed line: stable to the small eigenvalues but unstable to the large eigenvalues when $\tau \ll 1$. Dotted line: unstable to both the small and large eigenvalues when $\tau \ll 1$. Red dots are where the NLEP has a zero-eigenvalue crossing. In the right panel we have not shown the hairpin turn that occurs when $b \approx 1.67$ that provides the connection between an interior spike and a boundary spike solution.

and right panels of Fig. 9, these asymmetric solution branches are all linearly stable for τ sufficiently small with regards to the large eigenvalues for the range of values of H_+ between the two red dots shown in the right panel of Fig. 4 for $L = 3$ and of Fig. 1 for $L = 5$. Overall, this establishes a parameter regime where linearly stable asymmetric two-spike equilibria occur. For $L = 3$, this theoretical prediction of stable asymmetric two-spike equilibria is confirmed below in Fig. 12 of §5 from full PDE simulations of (1.1). For $L = 5$, a similar validation of the linear stability theory through full PDE simulations was given in Fig. 2 of §1.

In Fig. 5 we plot global bifurcation results for two-spike equilibria when $L = 10$. The right panel of Fig. 5 shows a parameter regime where stable asymmetric two-spike equilibria can occur when $\tau \ll 1$. However, in contrast to the global bifurcation diagrams when $L = 2, 3, 5$, we observe that when $L = 10$ there are two zero-crossings for the NLEP on each asymmetric solution branch, with the pattern being unstable to both the small and large eigenvalues for some intermediate range of b. This linear stability behavior with respect to the large eigenvalues is confirmed below in the left panel of Fig. 10 through numerical computations of the spectrum of a vector-valued NLEP. Moreover, we observe from Fig. 5 that asymmetric patterns originating from a symmetry-breaking bifurcation of symmetric two-spike equilibria are path-connected through a saddle-node point of high curvature to an unstable two-spike steady-state consisting of a boundary spike of large amplitude and an interior spike of small amplitude.

Similar results are shown in Fig. 6 for the infinite line problem where $L = \infty$. For this case, stable asymmetric patterns occur near the symmetry-breaking bifurcation point. Moreover, as for the case where $L = 10$, along the asymmetric solution branch there is an intermediate range of b where the pattern is unstable to both the small and large eigenvalues. This instability range of b for the large eigenvalues is observed

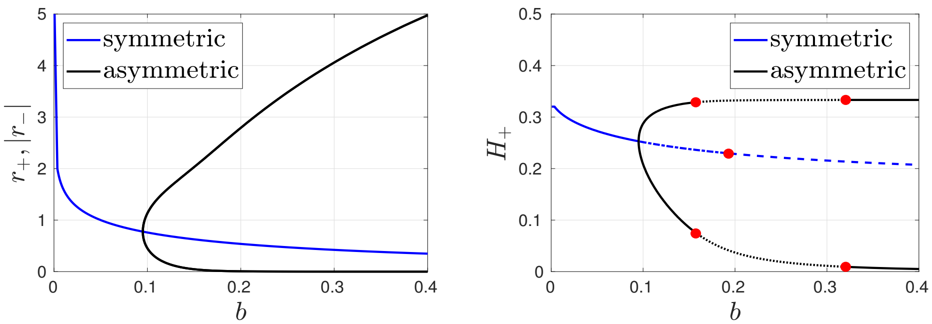

Fig. 6: Left: steady-state spike locations r_+ and $-r_-$ for $L = \infty$ versus b. Right: height H_+ of the rightmost spike versus b. Solid lines: linearly stable to both the small eigenvalues and the large (NLEP) eigenvalues when $\tau \ll 1$. Dash-dotted lines: unstable for the small eigenvalues but stable for the large eigenvalues when $\tau \ll 1$. Dashed line: stable to the small eigenvalues but unstable to the large eigenvalues when $\tau \ll 1$. Dotted line: unstable to both the small and large eigenvalues when $\tau \ll 1$. Red dots are where the NLEP has a zero-eigenvalue crossing. Observe that there is an intermediate range of b along the asymmetric branches where the pattern is unstable to both the small and large eigenvalues. The asymmetric patterns re-stabilize for larger b and results in a spike of large amplitude and another of negligible amplitude.

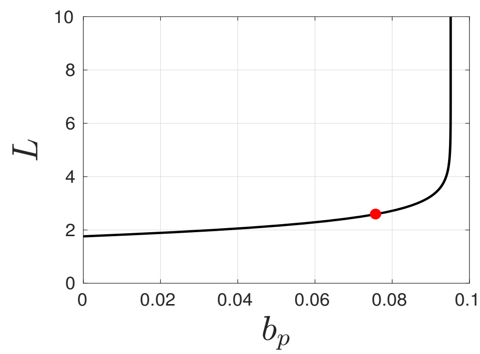

Fig. 7: Symmetry-breaking bifurcation point b_p versus L where the asymmetric branches of two-spike equilibria bifurcate from the symmetric branch. The red dot indicates the critical values $b_c \approx 0.0760$, $L_c \approx 2.597$, $r_{\pm,c} \approx 0.793$ where this bifurcation switches between subcritical and supercritical. The bifurcation curve has a vertical asymptote $b \approx 0.095$ as $L \to \infty$.

in Fig. 10 below from our computations of the spectra of the vector-valued NLEP. However, when $L = \infty$, there is no boundary spike solution and, as observed in Fig. 6, the asymmetric solution branch no longer terminates at a finite value of b.

3.3. Computation of a Degenerate Bifurcation Point. From the global bifurcation diagrams in Fig. 3 and Fig. 4 we observe that the symmetry-breaking bifurcation switches from subcritical to supercritical on the range $2 < L < 3$. We now describe a procedure to accurately compute the critical precursor parameter $b = b_c$ and critical domain half-length $L = L_c$ where this switch occurs. The significance of these critical values is that for $L > L_c$ the asymmetric solution branch is linearly stable with regards to the small eigenvalues near the bifurcation point.

To formulate our procedure for computing these critical values we first define

$$W(\ell) \equiv \xi(r_+(\ell), \ell) - \xi(r_-(\ell), -\ell)\,, \tag{3.19}$$

where $r_\pm = r_\pm(\ell)$ satisfy

$$f(r_\pm, \pm\ell) = 0\,.$$

Here $\xi(r, \ell)$ and $f(r, \ell)$ are defined in (3.10b). The asymmetric branch corresponds to a non-zero root of $W(\ell)$ and the symmetry-breaking bifurcation occurs when $W'(0) = 0$. To compute this point, denote $r = r_\pm(0)$, that is, the location of a symmetric spike which satisfies $f(r, 0) = 0$. Upon differentiating (3.19) implicitly and evaluating at $\ell = 0$ we obtain that $r'_-(0) = -r'_+(0) = -r'$, so that the bifurcation occurs when the following system is satisfied:

$$\ell = 0\,, \quad f = 0\,; \quad r' = -\frac{f_\ell}{f_r}\,; \quad \xi_r r' + \xi_\ell = 0\,. \tag{3.20}$$

In the left panel of Fig. 14 of Appendix A we include the Maple code that computes this bifurcation point. For example, when $L = 2$ we obtain from solving (3.20) that $b = 0.03406$ and $r = 0.835585$.

Since $W(\ell)$ is an odd function we have for small ℓ that

$$W(\ell) \sim \ell W'(0) + \ell^3 \frac{W'''(0)}{6} + O(\ell^5)\,,$$

with all even derivatives of W being zero. The criticality of the bifurcation depends on the sign of $W'''(0)$. A positive sign corresponds to a supercritical bifurcation, whereas a negative sign corresponds to a subcritical bifurcation. The change of bifurcation occurs when $W'''(0) = W'(0) = 0$. To compute $W'''(0)$, we differentiate implicitly and set $\ell = 0$. We readily calculate that

$$W'(0) = \xi_r r' + \xi_\ell\,, \qquad W''(0) = \xi_{rr} r'^2 + 2\xi_{r\ell} r' + \xi_r r'' + \xi_{\ell\ell}\,,$$
$$W'''(0) = \xi_{rrr} r'^3 + 3\xi_{rr\ell} r'^2 + 3\xi_{r\ell\ell} r' + 3\xi_{rr} r' r'' + 3\xi_{r\ell} r'' + \xi_r r''' + \xi_{\ell\ell\ell}\,.$$

The values of r, r' and r'' are obtained by differentiating f implicitly. This yields

$$r' = -\frac{f_\ell}{f_r}\,, \qquad r'' = -\frac{f_{rr} r'^2 + 2 f_{r\ell} r' + f_{\ell\ell}}{f_r}\,,$$
$$r''' = -\frac{f_{rrr} r'^3 + 3 f_{rr\ell} r'^2 + 3 f_{r\ell\ell} r' + 3 f_{rr} r' r'' + 3 f_{r\ell} r'' + f_{\ell\ell\ell}}{f_r}\,,$$

which are then evaluated at $\ell = 0$. In this way, the set of equations

$$l = 0\,, \quad f = 0\,; \quad W'(0) = 0\,, \quad W'''(0) = 0\,, \tag{3.21}$$

must be solved numerically to obtain the higher-order bifurcation point. The right panel of Fig. 14 of Appendix A shows the Maple implementation. Although the system

(3.21) is very large (its length is about 20,000 bytes in Maple), its numerical solution is found instantaneously, yielding

$$L = L_c \equiv 2.5972 \quad b = b_c \equiv 0.07596\,, \quad r = r_c \equiv .792655\,. \tag{3.22}$$

We conclude that the symmetry-breaking bifurcation is supercritical when $L > 2.5972$ and is subcritical when $L < 2.5972$.

4. NLEP Stability Analysis.

We now examine the stability on an $\mathcal{O}(1)$ time-scale of steady-state spike equilibria of (1.1), labeled by a_e and h_e. We will derive a new vector-valued nonlocal eigenvalue problem governing instabilities of the spike amplitudes on an $\mathcal{O}(1)$ time-scale. From this vector-NLEP, we will analyze in detail the linear stability of the two-spike equilibria constructed in §3 to these "large eigenvalues" for the choice $\mu = 1 + bx^2$.

To formulate the linear stability problem, we first introduce the perturbation

$$a(x,t) = a_e + e^{\lambda t}\phi(x)\,, \qquad h(x,t) = h_e + e^{\lambda t}\psi(x)\,, \tag{4.1}$$

into (1.1) and linearize. This leads to the singularly perturbed eigenvalue problem

$$\varepsilon^2\phi_{xx} - \mu(x)\phi + \frac{2a_e}{h_e}\phi - \frac{a_e^2}{h_e^2}\psi = \lambda\phi\,, \quad |x| \leq L\,; \qquad \phi_x(\pm L) = 0\,, \tag{4.2a}$$

$$\psi_{xx} - (1+\tau\lambda)\psi = -\frac{2}{\varepsilon}a_e\phi\,, \qquad |x| \leq L\,; \qquad \psi_x(\pm L) = 0\,. \tag{4.2b}$$

In the inner region near a spike at $x = x_j$, we have from (2.4) that

$$a_e \sim \mu_j H_j w\left(\sqrt{\mu_j}y_j\right) \quad h_e \sim H_j\,, \quad \text{where} \quad y_j = \varepsilon^{-1}(x - x_j)\,,$$

$\mu_j \equiv \mu(x_j)$, and $w(z) = \frac{3}{2}\operatorname{sech}^2(z/2)$. Here H_j is the spike height obtained from the steady-state of (2.22). Next, we introduce the localized eigenfunction

$$\Phi_j(y_j) = \phi(x_j + \varepsilon y_j)\,, \tag{4.3}$$

and obtain from (4.2a) that on $-\infty < y_j < \infty$, and for each $j = 1, \ldots, N$,

$$\frac{d^2\Phi_j}{dy_j^2} - \mu_j\Phi_j + 2\mu_j w\left(\sqrt{\mu_j}y_j\right)\Phi_j - \mu_j^2\left[w\left(\sqrt{\mu_j}y_j\right)\right]^2\Psi_j = \lambda\Phi_j\,, \tag{4.4}$$

where Ψ_j is a constant to be determined. Then, we let $z \equiv \sqrt{\mu_j}y$, and define $\hat{\Phi}_j(z) \equiv \Phi_j\left(z/\sqrt{\mu_j}\right)$, so that (4.4) becomes

$$\frac{d^2\hat{\Phi}_j}{dz^2} - \hat{\Phi}_j + 2w(z)\hat{\Phi}_j - \mu_j\left[w(z)\right]^2\Psi_j = \frac{\lambda}{\mu_j}\hat{\Phi}_j\,, \quad -\infty < z < \infty\,. \tag{4.5}$$

To determine Ψ_j, we must construct the outer solution for ψ in (4.2b). In the sense of distributions we calculate for $\varepsilon \to 0$ that

$$\frac{2}{\varepsilon}a_e\phi \to 2H_j\sqrt{\mu_j}\left(\int_{-\infty}^{\infty} w(z)\hat{\Phi}_j(z)\,dz\right)\delta(x - x_j)\,. \tag{4.6}$$

In this way, we obtain that the outer solution for ψ in (4.2b) satisfies

$$\psi_{xx} - \theta_\lambda^2 \psi = -2 \sum_{j=1}^{n} H_j \sqrt{\mu_j} \left(\int_{-\infty}^{\infty} w(z) \hat{\Phi}_j(z)\, dz \right) \delta(x - x_j)\,, \quad |x| \leq L\,, \tag{4.7a}$$

$$\psi_x(\pm L) = 0\,, \qquad \theta_\lambda \equiv \sqrt{1 + \tau\lambda}\,. \tag{4.7b}$$

In (4.7b) we must choose the principal branch of θ_λ. The constants Ψ_j for $j = 1, \ldots, N$ are obtained from the matching condition that $\Psi_j = \psi(x_j)$ for $j = 1, \ldots, N$.

By solving (4.7) on each subinterval we readily derive a linear algebraic system for $\mathbf{\Psi} \equiv (\Psi_1, \ldots, \Psi_N)^T$ in the form

$$\mathcal{B}_\lambda \mathbf{\Psi} = \frac{2}{\sqrt{1 + \tau\lambda}} \mathcal{U}^{1/2} \mathcal{H} \left(\int_{-\infty}^{\infty} w \mathbf{\Psi}\, dz \right)\,, \tag{4.8}$$

where the diagonal matrices $\mathcal{U}$ and $\mathcal{H}$ have diagonal entries $(\mathcal{U})_{jj} = \mu(x_j)$ and $(\mathcal{H})_{jj} = H_j$ for $j = 1, \ldots, N$. In (4.8), $\mathcal{B}_\lambda$ is defined by

$$\mathcal{B}_\lambda = \begin{pmatrix} c_{1\lambda} & d_{1\lambda} & & 0 \\ d_{1\lambda} & \ddots & \ddots & \\ & \ddots & \ddots & d_{N-1\lambda} \\ 0 & & d_{N-1\lambda} & c_{N\lambda} \end{pmatrix}\,, \tag{4.9a}$$

where the matrix entries are given by

$$\begin{aligned} c_{1\lambda} &= \coth(\theta_\lambda(x_2 - x_1)) + \tanh(\theta_\lambda(L + x_1))\,, \\ c_{N\lambda} &= \coth(\theta_\lambda(x_N - x_{N-1})) + \tanh(\theta_\lambda(L - x_N))\,, \\ c_{j\lambda} &= \coth(\theta_\lambda(x_{j+1} - x_j)) + \coth(\theta_\lambda(x_j - x_{j-1}))\,, \quad j = 2, \ldots N-1\,, \\ d_{j\lambda} &= -\operatorname{csch}(\theta_\lambda(x_{j+1} - x_j))\,, \quad j = 1, \ldots, N-1\,. \end{aligned} \tag{4.9b}$$

Next, upon substituting (4.8) into (4.5), we obtain the following vector-valued NLEP for $\hat{\mathbf{\Phi}} \equiv (\hat{\Phi}_1, \ldots, \hat{\Phi}_N)^T$ on $-\infty < z < \infty$;

$$\mathcal{L}\hat{\mathbf{\Phi}} - w^2 \frac{\int_{-\infty}^{\infty} w \mathcal{E}_\lambda \hat{\mathbf{\Phi}}\, dz}{\int_{-\infty}^{\infty} w^2\, dz} = \lambda \mathcal{U}^{-1} \hat{\mathbf{\Phi}}\,; \qquad \hat{\mathbf{\Phi}} \to \mathbf{0} \quad \text{as } |z| \to \infty\,, \tag{4.10a}$$

$$\mathcal{E}_\lambda \equiv \frac{12}{\sqrt{1 + \tau\lambda}} \mathcal{U} \mathcal{B}_\lambda^{-1} \mathcal{U}^{-1} \left(\mathcal{U}^{3/2} \mathcal{H} \right)\,, \qquad \mathcal{L}\hat{\mathbf{\Phi}} \equiv \hat{\mathbf{\Phi}}'' - \hat{\mathbf{\Phi}} + 2w\hat{\mathbf{\Phi}}\,. \tag{4.10b}$$

We then diagonalize $\mathcal{E}_\lambda$ by finding the eigenvalues $\mathcal{E}_\lambda \boldsymbol{e} = \chi_\lambda \boldsymbol{e}$ and obtain that

$$\mathcal{E}_\lambda = \mathcal{V} \Lambda \mathcal{V}^{-1}\,, \tag{4.11}$$

where $\mathcal{V}$ is the matrix of eigenvectors of $\mathcal{E}_\lambda$ and Λ is the diagonal matrix of eigenvalues with $(\Lambda)_{jj} = \chi_{\lambda,j}$, for $j = 1, \ldots, N$. Then, by defining $\tilde{\mathbf{\Phi}} = \mathcal{V}^{-1} \hat{\mathbf{\Phi}}$, we obtain the following vector-valued NLEP defined on $-\infty < z < \infty$ with $\tilde{\mathbf{\Phi}} \to 0$ as $|z| \to \infty$:

$$\mathcal{L}\tilde{\mathbf{\Phi}} - w^2 \Lambda \frac{\int_{-\infty}^{\infty} w \tilde{\mathbf{\Phi}}\, dz}{\int_{-\infty}^{\infty} w^2\, dz} = \lambda \mathcal{C} \tilde{\mathbf{\Phi}}\,; \qquad \mathcal{C} \equiv \mathcal{V}^{-1} \mathcal{U}^{-1} \mathcal{V}\,. \tag{4.12}$$

The key difference between this NLEP analysis and that for the Gierer-Meinhardt model with no precursor field in [15] and [14] is that the NLEP cannot be diagonalized into N separate scalar NLEPs, one for each eigenvalue of Λ. From (4.12) we observe that the NLEPs are coupled through the matrix $\mathcal{C}$.

We now study (4.12) for our two-spike symmetric and asymmetric equilibria constructed in §3 for $\mu = 1 + bx^2$.

4.1. NLEP Analysis: Symmetric 2-Spike Equilibria. For the symmetric two-spike case with $x_2 = -x_1$, we use $\mathcal{U} = \mu(x_2)I$ and $\mathcal{H} = H_c I$, to get from (4.10b) that

$$\mathcal{E}_\lambda = \frac{12}{\sqrt{1+\tau\lambda}} \left[\mu(x_2)\right]^{3/2} H_c \mathcal{B}_\lambda^{-1}\,, \quad \text{where} \quad \left[\mu(x_2)\right]^{3/2} H_c = \tanh(x_2) + \tanh(L - x_2)\,, \tag{4.13}$$

as obtained from (3.8). We readily calculate the matrix spectrum of $\mathcal{B}_\lambda$ as

$$\begin{aligned} &\mathcal{B}_\lambda \boldsymbol{v}_1 = \kappa_{1\lambda}\boldsymbol{v}_1\,; \quad \boldsymbol{v}_1 = (1,1)^T\,, \quad \kappa_{1\lambda} \equiv \tanh(\theta_\lambda x_2) + \tanh(\theta_\lambda(L-x_2))\,,\\ &\mathcal{B}_\lambda \boldsymbol{v}_2 = \kappa_{2\lambda}\boldsymbol{v}_2\,; \quad \boldsymbol{v}_2 = (1,-1)^T\,, \quad \kappa_{2\lambda} \equiv \coth(\theta_\lambda x_2) + \tanh(\theta_\lambda(L-x_2))\,. \end{aligned} \tag{4.14}$$

In this way, for symmetric two-spike equilibria, we obtain that (4.12) is equivalent to the two scalar NLEPs, with NLEP *multipliers* $\chi_{1,\lambda}$ and $\chi_{2,\lambda}$, defined by

$$\mathcal{L}\tilde{\boldsymbol{\Phi}} - w^2 \Lambda \frac{\int_{-\infty}^{\infty} w \tilde{\boldsymbol{\Phi}}\, dz}{\int_{-\infty}^{\infty} w^2\, dz} = \frac{\lambda}{\left[\mu(x_2)\right]^{3/2}} \tilde{\boldsymbol{\Phi}}\,, \quad -\infty < z < \infty\,; \quad \tilde{\boldsymbol{\Phi}} \to 0 \quad \text{as} \quad |z| \to \infty\,; \tag{4.15a}$$

$$(\Lambda)_{11} \equiv \chi_{1,\lambda} = \frac{2}{\sqrt{1+\tau\lambda}} \left(\frac{\tanh(x_2) + \tanh(L-x_2)}{\tanh(\theta_\lambda x_2) + \tanh(\theta_\lambda(L-x_2))} \right)\,, \tag{4.15b}$$

$$(\Lambda)_{22} \equiv \chi_{2,\lambda} = \frac{2}{\sqrt{1+\tau\lambda}} \left(\frac{\tanh(x_2) + \tanh(L-x_2)}{\coth(\theta_\lambda x_2) + \tanh(\theta_\lambda(L-x_2))} \right)\,, \tag{4.15c}$$

where $\theta_\lambda = \sqrt{1+\tau\lambda}$.

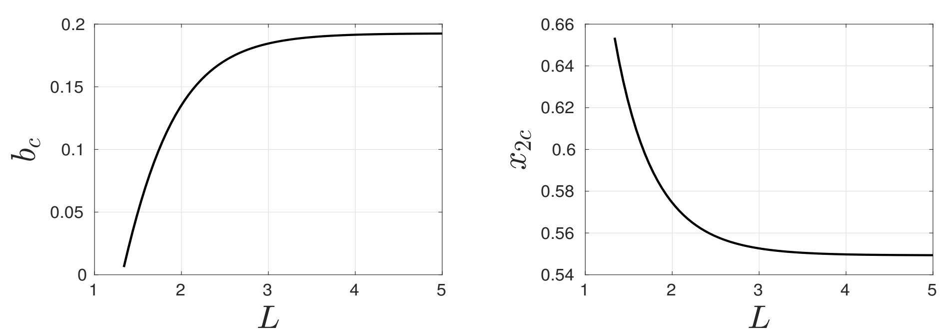

Fig. 8: Critical values b_c of the precursor parameter b (left panel) and the spike location x_{2c} (right panel) versus L where the NLEP (4.15) with multiplier $\chi_{2,\lambda}$ has a zero-eigenvalue crossing for the linearization of a symmetric two-spike steady-state. For $x_2 < x_{2c}$, or equivalently for $b > b_c$, a competition instability on an $\mathcal{O}(1)$ time-scale occurs.

We first consider the *competition mode* corresponding to $\boldsymbol{v}_2 = (1, -1)^T$ where the multiplier of the NLEP in (4.15a) is $\chi_{2,\lambda}$, which depends on λ through the product $\tau\lambda$, so that $\chi_{2,\lambda} = \chi_{2,\lambda}(\tau\lambda)$. From Proposition 3.6 of [24], we conclude for this competition mode that there is a unique eigenvalue in $\mathrm{Re}(\lambda) > 0$ for any $\tau > 0$ when $\chi_{2,\lambda}(0) < 2$. By using (4.15c), we calculate that $\chi_{2,\lambda}(0) < 2$ when

$$2\tanh(x_2) + 2\tanh(L - x_2) < \coth(x_2) + \tanh(L - x_2)\,,$$

which, after some algebra, reduces to

$$\coth(x_2)\coth(L) > 2 \qquad \Longrightarrow \qquad 0 < x_2 < x_{2c} \equiv \frac{1}{2}\log\left(\frac{2+\coth L}{2-\coth L}\right)\,, \tag{4.16}$$

provided that $L > L_c \equiv \log(2+\sqrt{3}) \approx 1.3169$. We conclude that a competition instability occurs whenever spikes become too close. When $L < L_c$, a competition instability occurs for any $x_2 > 0$. Equivalently, from (3.7), we conclude that on the range $L > L_c$ a competition instability occurs along the symmetric branch of equilibria whenever the precursor parameter b satisfies $b > b_c$, where

$$b_c = \frac{[\tanh(L - x_{2c}) - \tanh(x_{2c})]}{x_{2c}\left(5 - x_{2c}\left[\tanh(L - x_{2c}) - \tanh(x_{2c})\right]\right)}\,. \tag{4.17}$$

In Fig. 8 we plot b_c and x_{2c} versus L on the range $L > L_c \approx 1.3169$. Numerical values for b_c for different L correspond to the red dots on the symmetric branches of equilibria shown in Fig. 1, and in Figs. 3, 4, 5, 6. For $b < b_c$, or equivalently for $x_2 > x_{2c}$, Proposition 3.6 of [24] can be used to prove that the two-spike symmetric steady-state is linearly stable on $\mathcal{O}(1)$ time-scales whenever τ in (1.1) is below a Hopf bifurcation threshold τ_H. We refer the reader to [24] for the proof of this statement.

Next, we briefly consider the NLEP (4.15) for the synchronous mode $\boldsymbol{v}_1 = (1, 1)^T$, where the NLEP multiplier $\chi_{1,\lambda}$ is given in (4.15b). We calculate that $\chi_{1,\lambda}(0) = 2$, for any $\tau > 0$ and $b > 0$. As a result, from Theorem 2.4 of [28] (see also [30]) we conclude that the NLEP for the synchronous mode has no eigenvalues in $\mathrm{Re}(\lambda) > 0$ when $\tau = 0$, or when τ is sufficiently small. As similar to the analysis in [28] with no precursor, a Hopf bifurcation can occur when τ exceeds a threshold, which now depends on b and L. We do not calculate this Hopf point numerically here.

We summarize our NLEP stability result for the symmetric two-spike steady-state branch as follows:

Proposition 1. *Consider the two-spike symmetric steady-state solution for* (1.1) *with precursor $\mu(x) = 1 + bx^2$, where the spike locations x_1 and x_2, with $x_2 = -x_1$ are given in terms of b by* (3.7)*. Suppose that $L > L_c \equiv \log(2+\sqrt{3}) \approx 1.3169$ and define the critical half-distance x_{2c} between the spikes and the critical precursor parameter b_c by* (4.16) *and* (4.17)*, respectively. Then, for any b with $b > b_c$, or equivalently for any x_2 with $x_2 < x_{2c}$, the NLEP* (4.15) *with multiplier $\chi_{2,\lambda}$ for the competition mode has a unique unstable eigenvalue in $Re(\lambda) > 0$. Alternatively, if $b < b_c$, and for $0 \leq \tau < \tau_H$, the two-spike symmetric steady-state is linearly stable on $\mathcal{O}(1)$ time-scales to the competition mode. Finally, the NLEP* (4.15) *for the synchronous mode, with multiplier $\chi_{1,\lambda}$, has no unstable eigenvalues when $\tau > 0$ is sufficiently small.*

4.2. NLEP Analysis: Asymmetric 2-Spike Equilibria. We will analyze the NLEP (4.10) for two-spike asymmetric equilibria for the special case where $\tau = 0$. To do so, we set $\mathcal{F}_3 = \mathcal{F}_4 = 0$ in (3.1) to calculate that

$$\mathcal{U}^{3/2}\mathcal{H} = \mathcal{Z}\,, \qquad \text{where} \qquad \mathcal{Z} \equiv \frac{1}{6}\begin{pmatrix} c_1 + d_1 s & 0 \\ 0 & c_2 + d_1/s \end{pmatrix}, \tag{4.18}$$

with $s = H_2/H_1$. As a result, since $\mathcal{U}$ and $\mathcal{Z}$ are diagonal matrices, we can write the NLEP in (4.10) when $\tau = 0$ as

$$\mathcal{L}\hat{\boldsymbol{\Phi}} - w^2 \frac{\int_{-\infty}^{\infty} w \mathcal{E}_\lambda \hat{\boldsymbol{\Phi}}\, dz}{\int_{-\infty}^{\infty} w^2\, dz} = \lambda \mathcal{U}^{-1}\hat{\boldsymbol{\Phi}}\,; \qquad \mathcal{E}_\lambda \equiv 2\mathcal{U}\mathcal{B}_\lambda^{-1}\mathcal{Z}\mathcal{U}^{-1}\,. \tag{4.19}$$

Next, upon defining $\mathcal{A}$ by $\mathcal{A} = \mathcal{Z}^{-1}\mathcal{B}_\lambda$, we calculate its matrix spectrum $\mathcal{A}\boldsymbol{v} = \kappa\boldsymbol{v}$, which can be written as $\mathcal{B}_\lambda \boldsymbol{v} = \kappa \mathcal{Z}\boldsymbol{v}$. By using (4.9) for $\mathcal{B}_\lambda$ with $\tau = 0$, and (4.18) for $\mathcal{Z}$, we conclude that κ must satisfy

$$\det\begin{pmatrix} c_1 - \kappa(c_1 + d_1 s) & d_1 \\ d_1 & c_2 - \kappa\left(c_2 + \frac{d_1}{s}\right) \end{pmatrix} = 0\,, \tag{4.20a}$$

which yields that κ satisfies the quadratic equation

$$\kappa^2\left(c_1c_2 + c_2 d_1 s + d_1^2 + \frac{c_1 d_1}{s}\right) - \kappa\left(2c_1c_2 + d_1 s c_2 + \frac{d_1 c_1}{s}\right) + c_1c_2 - d_1^2 = 0\,. \tag{4.20b}$$

Observe that $\kappa_1 = 1$ is always an eigenvalue, and so κ_2 can readily be found. A simple calculation yields that the matrix spectrum of $\mathcal{Z}^{-1}\mathcal{B}_\lambda$ is

$$\begin{aligned} &\kappa_1 = 1\,, \quad \boldsymbol{v}_1 = \begin{pmatrix} 1 \\ s \end{pmatrix}, \\ &\kappa_2 = \frac{c_1c_2 - d_1^2}{c_1c_2 + d_1^2 + d_1\left(c_2 s + c_1/s\right)}\,, \quad \boldsymbol{v}_2 = \begin{pmatrix} -d_1 \\ c_1 - \kappa_2(c_1 + d_1 s) \end{pmatrix}. \end{aligned} \tag{4.21}$$

Next, we define the eigenvector matrix $\mathcal{V}$, the diagonal matrix Λ, and the matrix $\mathcal{C}$ by

$$\mathcal{V} \equiv \begin{pmatrix} 1 & -d_1 \\ s & c_1 - \kappa_2(c_1 + d_1 s) \end{pmatrix}, \qquad \Lambda \equiv \begin{pmatrix} 2 & 0 \\ 0 & 2/\kappa_2 \end{pmatrix}, \qquad \mathcal{C} \equiv \mathcal{V}^{-1}\mathcal{U}^{-1}\mathcal{V}\,, \tag{4.22}$$

so that $\mathcal{E}_\lambda = 2\mathcal{U}\mathcal{A}^{-1}\mathcal{U}^{-1} = (\mathcal{U}\mathcal{V})\,\Lambda\,(\mathcal{U}\mathcal{V})^{-1}$. Finally, by setting $\tilde{\boldsymbol{\Phi}} = (\mathcal{U}\mathcal{V})^{-1}\hat{\boldsymbol{\Phi}}$, we obtain the vector-valued NLEP (4.12), where Λ and $\mathcal{C}$ are defined explicitly in (4.22).

In the context of spike stability, the vector-valued NLEP (4.12) is a new linear stability problem, for which the NLEP stability results for the scalar case in [30], [28], and [4] are not directly applicable. Analytically, it is challenging to provide necessary and sufficent conditions to guarantee that the NLEP (4.12) has no eigenvalues in $\mathrm{Re}(\lambda) > 0$. However, one can analyze any zero-eigenvalue crossings, by using the well-known identity $L_0 w = w^2$. By setting $\tilde{\boldsymbol{\Phi}} = (0, w)^T$, we observe from (4.12) that a zero-eigenvalue crossing will occur when $\kappa_2 = 2$. By using (4.21) for κ_2, a zero-eigenvalue crossing occurs when

$$c_1c_2 + 3d_1^2 = 2|d_1|\left(c_2 s + \frac{c_1}{s}\right). \tag{4.23}$$

Here c_1, c_2 and d_1 are determined in terms of the steady-state spike locations x_1 and x_2 by (3.5), while $s = H_2/H_1$ parameterizes the branch of asymmetric two-spike equilibria in either (3.4), or equivalently (3.9). An interpretation of the zero-eigenvalue crossing is given in the following remark.

Remark 4.1. Equilibria of the DAE system (2.22) are solutions to the nonlinear algebraic system $\mathcal{F}(x_1, x_2, H_1, H_2) = \mathbf{0}$ for $\mathcal{F} \in \mathbb{R}^4$, as given in (3.1). For a fixed x_1 and x_2, we claim that the linearization of the subsystem $\mathcal{F}_3 = \mathcal{F}_4 = 0$ in (3.1) for the spike amplitudes is not invertible when the NLEP has a zero-eigenvalue crossing. To see this, we calculate along solutions to (3.1) that

$$\begin{aligned} J_3 &\equiv \begin{pmatrix} \mathcal{F}_{3H_1} & \mathcal{F}_{3H_2} \\ \mathcal{F}_{4H_1} & \mathcal{F}_{4H_2} \end{pmatrix} \\ &= \begin{pmatrix} 12\mu_1^{3/2} H_1 - c_1 & -d_1 \\ -d_1 & 12\mu_2^{3/2} H_2 - c_2 \end{pmatrix} = \begin{pmatrix} c_1 + 2d_1 s & -d_1 \\ -d_1 & c_2 + 2d_1/s \end{pmatrix} . \end{aligned}$$

A simple calculation shows that $\det(J_3) = 0$ if and only if

$$c_1 c_2 + 3d_1^2 = -2d_1 \left(c_2 s + \frac{c_1}{s} \right) , \tag{4.24}$$

which is the condition derived in (4.23) for the zero-eigenvalue crossing of the NLEP.

The condition (4.23) for a zero-eigenvalue crossing is indicated by the red dots on the asymmetric branches of equilibria shown in Fig. 1, and in Figs. 3, 4, 5, 6. For the corresponding scalar NLEP case, where $\mathcal{C}$ is a multiple of the identity, the rigorous results of [30] prove that $\text{Re}(\lambda) \leq 0$ if and only if $\kappa_2 < 2$, and that an unstable real eigenvalue exists if $\kappa_2 > 2$. We now investigate numerically whether these optimal linear stability results persist for the vector-valued NLEP.

4.2.1. Numerical Computation of the Vector-Valued NLEP. We compute the discrete eigenvalues of the vector-valued NLEP (4.12) for $\tilde{\mathbf{\Phi}} \equiv \left(\tilde{\Phi}_1, \tilde{\Phi}_2\right)^T$, where Λ and $\mathcal{C}$ are defined in (4.22). To do so, we use a second-order centered finite difference discretization of the NLEP, where the nonlocal term is discretized using the trapezoidal rule. We discretize (4.12) on $0 \leq z \leq z_M$ using the nodal values

$$\begin{gathered} z_j = h(j-1) , \quad h \equiv \frac{z_M}{n-1} , \quad w_j = w(z_j) = \frac{3}{2} \text{sech}^2 \left(\frac{z_j}{2} \right) , \quad j = 1, \ldots, n , \\ \mathbf{\Psi} \equiv (\Psi_{1,1}, \ldots, \Psi_{1,n}, \Psi_{2,1}, \ldots, \Psi_{2,n})^T , \end{gathered}$$

where $\Psi_{1,j} \approx \tilde{\Phi}_1(z_j)$ and $\Psi_{2,j} \approx \tilde{\Phi}_2(z_j)$ for $j = 1, \ldots, n$. We impose that $\tilde{\mathbf{\Phi}}' = 0$ at $z = 0, z_M$, which is discretized by centered differences. The resulting block-structured matrix eigenvalue problem for the pair $\mathbf{\Psi} \in \mathbb{R}^{2n}$ and λ is given by

$$(\mathcal{K}_n + \mathcal{M}_n) \mathbf{\Psi} = \lambda \mathcal{P}_n \mathbf{\Psi} , \tag{4.25a}$$

where the matrices $\mathcal{K}_n \in \mathbb{R}^{2n,2n}$, $\mathcal{M}_n \in \mathbb{R}^{2n,2n}$ and $\mathcal{P}_n \in \mathbb{R}^{2n,2n}$, are defined by

$$\mathcal{K}_n \equiv \begin{pmatrix} \mathcal{K} & 0 \\ 0 & \mathcal{K} \end{pmatrix} , \quad \mathcal{M}_n \equiv \begin{pmatrix} \mathcal{M} & 0 \\ 0 & \kappa_2^{-1} \mathcal{M} \end{pmatrix} , \quad \mathcal{P}_n \equiv \begin{pmatrix} c_{11} I & c_{12} I \\ c_{21} I & c_{22} I \end{pmatrix} . \tag{4.25b}$$

Here $I \in \mathbb{R}^{n,n}$ is the identity, and c_{ij} for $1 \leq i, j \leq 2$ are the matrix entries of the 2×2 matrix $\mathcal{C}$ defined in (4.22). In (4.25b), the $n \times n$ tridiagonal matrix $\mathcal{K}$ and the full $n \times n$ matrix $\mathcal{M}$ are defined, respectively, by

$$\begin{gathered} \mathcal{K}_{1,2} = \mathcal{K}_{n,n-1} = \frac{2}{h^2} , \quad \mathcal{K}_{ii} = -\frac{2}{h^2} - 1 + 2w_i , \quad \text{for} \quad i = 1, \ldots n , \\ \mathcal{K}_{i,i+1} = \mathcal{K}_{i,i-1} = \frac{1}{h^2} , \quad \text{for} \quad i = 2, \ldots, n-1 , \end{gathered} \tag{4.25c}$$

and

$$\mathcal{M} \equiv -\frac{2h}{3} \begin{pmatrix} w_1^2 \left(\frac{w_1}{2}\right) & w_1^2 w_2 & \dots & w_1^2 w_{n-1} & w_1^2 \left(\frac{w_n}{2}\right) \\ \vdots & \vdots & \vdots & \vdots & \vdots \\ \vdots & \vdots & \vdots & \vdots & \vdots \\ w_n^2 \left(\frac{w_1}{2}\right) & w_n^2 w_2 & \dots & w_n^2 w_{n-1} & w_n^2 \left(\frac{w_n}{2}\right) \end{pmatrix}. \tag{4.25d}$$

For $n = 250$ and $z_M = 15$, the matrix spectrum of (4.25) is computed numerically using a generalized matrix eigenvalue solver from EISPACK at each point along the asymmetric solution branches of two-spike equilibria. In Fig. 9 we plot the first two eigenvalues of (4.25), defined as those with the largest real parts, versus the height H_+ of the rightmost spike for $L = 2, 3, 5$. In terms of H_+, we recall that the asymmetric branches of equilibria for these values of L were shown in the right panels of Figs. 3, 4 and 1, respectively. From Fig. 9 we observe that the first two eigenvalues are real-valued except for a small range of H_+ when $L = 2$, where they form a complex conjugate pair. These numerical results confirm the zero-eigenvalue crossing condition (4.23), obtained by setting $\kappa_2 = 2$, as evidenced by the intersection of the heavy-solid curves and the horizontal blue lines in Fig. 9. However, most importantly, the results in Fig. 9 establish numerically that the vector-valued NLEP (4.12), which is valid for $\tau = 0$, has no unstable discrete eigenvalues whenever $\kappa_2 < 2$, and that there is a unique unstable discrete eigenvalue when $\kappa_2 > 2$. Increasing the number of gridpoints n or the cutoff z_M did not alter the results to two decimal places of accuracy.

For $L = 10$ and for the infinite domain problem with $L = \infty$, in Fig. 10 we plot the first two eigenvalues of (4.25) versus the precursor parameter b along the asymmetric solution branches of Fig. 5 and Fig. 6. From Fig. 10 we observe that along these solution branches the NLEP has two zero-eigenvalue crossings, corresponding to where $\kappa_2 = 2$, and that the vector NLEP has a unique unstable eigenvalue between these crossings. This linear stability behavior is encoded in the global bifurcation diagrams for $L = 10$ and $L = \infty$ shown in the right panels of Fig. 5 and Fig. 6, respectively.

5. Validation from PDE Simulations. In this section, we validate our global bifurcation and linear stability results for the precursor field $\mu(x) = 1+bx^2$ from time-dependent PDE simulations of (1.1). In our simulations, we give initial conditions for (1.1) that correspond to a two-spike quasi-equilibrium solution, where the spike heights satisfy the constraint in (2.22) for given spike locations x_1 and x_2 at $t = 0$.

For $L = 5$ and $b = 0.12$, the results from the PDE simulations shown in Fig. 2 confirm that a quasi-equilibrium two-spike pattern tends to a stable asymmetric two-spike equilibrium on a long time scale, as predicted by the bifurcation diagram shown in the right panel of Fig. 1. The other parameter values are shown in caption of Fig. 2. In contrast, if $b = 0.18$, from the PDE simulation results shown in Fig. 11 we observe that a two-spike quasi-equilibrium solution undergoes a competition instability leading to the destruction of a spike. For this parameter set, there is no stable asymmetric two-spike steady-state pattern as observed from the right panel of Fig. 1.

Similarly, for $L = 3$ and $b = 0.09$, we observe from the full numerical results shown in Fig. 12 that the quasi-equilibrium two-spike pattern converges as t increases to a stable asymmetric steady-state pattern. As shown in the bifurcation diagram given in the right panel of Fig. 4 there is a stable asymmetric two-spike steady-state for these parameter values.

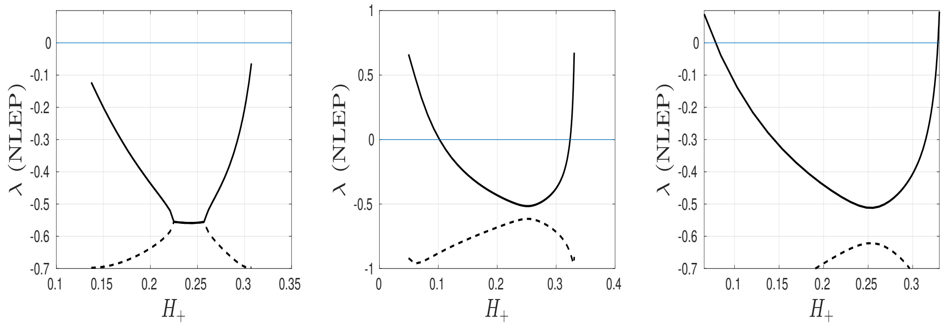

Fig. 9: Plot of the first (heavy solid) and second (dashed) eigenvalues (ordered by the largest real parts), as computed from the discretization of the vector-valued NLEP (4.12) versus the height H_+ of the rightmost spike along the asymmetric solution branches shown in Figs. 3, 4 and 1 for domain half-lengths $L = 2$ (left), $L = 3$ (middle) and $L = 5$ (right), respectively. Numerical evidence shows that when $\kappa_2 < 2$, the vector NLEP has no unstable eigenvalues, and that a unique positive eigenvalue occurs when $\kappa_2 > 2$. Here κ_2 is defined in (4.21) and the zero-eigenvalue crossing occurs when $\kappa_2 = 2$, leading to (4.23). The thin horizontal blue line is the zero-eigenvalue crossing.

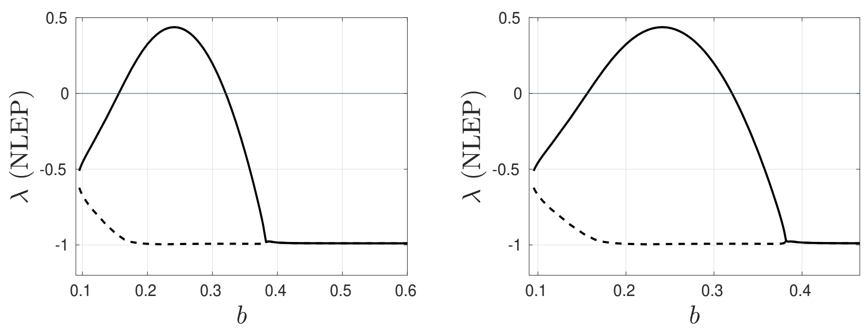

Fig. 10: Plot of the first (heavy solid) and second (dashed) eigenvalues (ordered by the largest real parts), as computed from the discretization of the vector-valued NLEP (4.12) versus the precursor parameter b along the asymmetric solution branches shown in Figs. 5 and 6 for a domain half-length $L = 10$ (left panel) and an infinite domain $L = \infty$ (right panel), respectively. The NLEP has two zero-eigenvalue crossings (intersection with the horizontal blue line) on each portion of the asymmetric branch at parameter values where $\kappa_2 = 2$ (see Fig. 5 and Fig. 6). Between the zero-eigenvalue crossings the vector NLEP has a unique unstable real eigenvalue.

Finally, for $L = 10$, in Fig. 13 we show results for two-spike solutions computed from PDE simulations of (1.1) for $b = 0.15$ and for $b = 0.20$. In the left panel of Fig. 13 we show a stable asymmetric two-spike steady-state for $b = 0.15$ as computed numerically from (1.1), starting from an initial condition chosen to be close to the stable asymmetric pattern predicted from the global bifurcation diagram in Fig. 5.

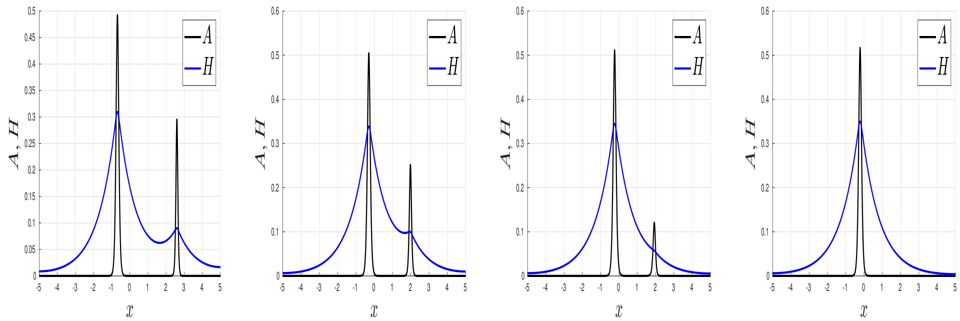

Fig. 11: Time-dependent PDE simulations of (1.1) with $L = 5$, $\varepsilon = 0.05$, and $\tau = 0.25$ for a precursor $\mu(x) = 1 + bx^2$ with $b = 0.18$. Initial condition is a quasi-equilibrium two-spike solution with spike locations $x_1(0) = -1$ and $x_2(0) = 3$. Plots of A and H versus x at four different times showing that one spike is annihilated as time increases. For $b = 0.18$, the right panel in Fig. 1 shows that there is no stable asymmetric two-spike pattern. Left: $t = 180$. Left Middle: $t = 335$. Right Middle: $t = 650$. Right: $t = 800$.

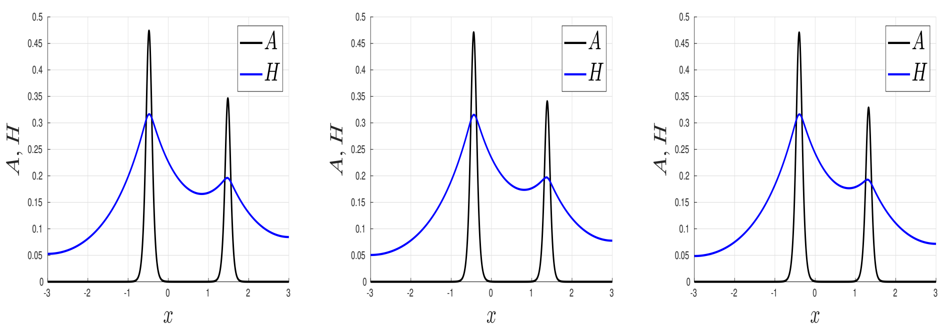

Fig. 12: Time-dependent PDE simulations of (1.1) with $L = 3$, $\varepsilon = 0.05$, and $\tau = 0.15$ for a precursor $\mu(x) = 1 + bx^2$ with $b = 0.09$. Initial condition is a quasi-equilibrium two-spike solution with spike locations $x_1(0) = -0.5$ and $x_2(0) = 1.5$. Plots of A and H versus x at three different times showing the convergence towards a stable asymmetric two-spike pattern as predicted from the right panel of Fig. 4. Left: $t = 31$. Middle: $t = 301$. Right: $t = 900$. As t increases there is only a slight adjustment of the pattern.

For $b = 0.20$, where no such stable asymmetric pattern exists from Fig. 5, the PDE simulations shown in the other three panels in Fig. 13 confirm the instability and show the annihilation of the small spike as time increases.

6. Discussion. For the GM model (1.1) with a precursor field $\mu(x) = 1 + bx^2$, we have shown that a linearly stable asymmetric two-spike steady-state pattern can emerge from a supercritical pitchfork bifurcation at some critical value of b along a symmetric branch of two-spike equilibria. For this symmetry-breaking bifurcation, the critical value of b depends on the domain half-length L. From a linearization around

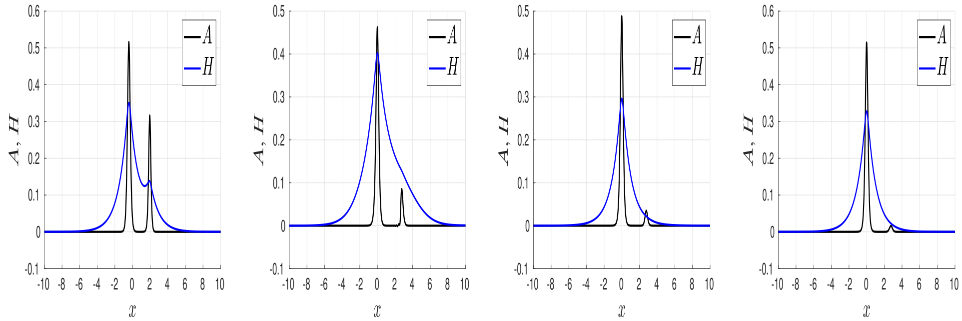

Fig. 13: Left panel: steady-state of time-dependent PDE simulations of (1.1) with $L = 10$, $\varepsilon = 0.10$, and $\tau = 0.15$ for $\mu(x) = 1 + bx^2$ with $b = 0.15$. Other panels: PDE simulations of (1.1) when b is increased to $b = 0.20$ (other parameters the same). For $b = 0.20$, the NLEP stability theory in Fig. 10 predicts no stable asymmetric two-spike steady-state. The PDE numerical results show a collapse of the small spike. Left middle: $t = 0$. Right middle: $t = 0.61$. Right: $t = 1.2$. For the PDE simulations with $b = 0.15$ and $b = 0.20$, the initial condition was a 2% perturbation of the asymmetric steady state shown in the global bifurcation diagram Fig. 5.

the steady-state of a DAE system of ODEs for the spike locations and spike heights, we have shown numerically that some portions of the asymmetric branches of equilibria are linearly stable to the small eigenvalues. Moreover, from a combined analytical and numerical investigation of the spectrum of a novel class of vector-valued NLEP, we have shown that portions of the branches of asymmetric two-spike equilibria are linearly stable to $\mathcal{O}(1)$ time-scale spike amplitude instabilities. Overall, our combined analytical and numerical study establishes the qualitatively novel result that linearly stable asymmetric two-spike equilibria can occur for the GM model with a precursor field. Asymmetric two-spike equilibria in 1-D for the GM model are all unstable in the absence of a precursor field [29].

Although we have only exhibited stable asymmetric patterns for the GM model with a specific precursor field with two spikes, the analytical framework we have employed applies to multiple spikes, to other precursor fields, and to other singularly perturbed RD systems. In particular, the equilibria of the DAE system (2.18) could be used to compute the bifurcation diagram of symmetric and asymmetric spike equilibria for more than two spikes.

There are two open directions that warrant further investigation. One specific focus would be to extend NLEP stability theory for scalar NLEPs to establish analytically necessary and sufficient conditions for the vector-valued NLEP (4.12) to admit no eigenvalues in $\mathrm{Re}(\lambda) > 0$. In this NLEP we would allow $\mathcal{C}$ in (4.12) to be an arbitrary matrix with positive eigenvalues. A second open direction would be to extend the 1-D theory for the GM model with a precursor field to a 2-D setting in order to construct stable asymmetric spot patterns in a 2-D domain.

7. Acknowledgements. Theodore Kolokolnikov and Michael Ward were supported by NSERC Discovery grants. Frédéric Paquin-Lefebvre was supported by a UBC Four-Year Graduate Fellowship.

Appendix A. Alternative Formulation of Two-Spike Equilibria.

In this appendix we briefly outline the derivation of the coupled system (3.10) characterizing two-spike equilibria for the special case where $\mu(x)$ is even in x. We center the spikes at $x_2 = r_+$ and $x_1 = -r_-$, and we let ℓ be the unknown location, with $x_1 < \ell < x_2$, where $h_x(\ell) = a_x(\ell) = 0$. We label the spike heights as $H_\pm = h(\pm r_\pm)$.

To proceed, we first construct a steady-state spike at $x = r_+$ on the interval (ℓ, L) with $h_x = 0$ and $a_x = 0$ at $x = \ell, L$. A similar construction is made for the interval $(-L, \ell)$ with a spike at $x = -r_-$. Then, since $\mu(x)$ is even, we can write the two steady-state conditions in a compact unified form, with the remaining equation resulting from adjusting $h(\ell)$ so that $h(x)$ is continuous across $x = \ell$.

For the right interval $\ell < x < L$ with a spike at $x = r_+$, we proceed as in the derivation of (2.16) to obtain that r_+ satisfies

$$\text{(A.1)} \qquad -\frac{\mu'(r_+)}{\mu(r_+)} - \frac{4}{5}\frac{\langle g_{1x}\rangle|_{x=r_+}}{g_1|_{x=r_+}} = 0\,,$$

where $\langle g_{1x}\rangle$ is the average of g_{1x} across $x = r_+$. Here $g_1(x, r_+)$ is the 1-D Green's function satisfying

$$\text{(A.2)} \qquad g_{1xx} - g_1 = -\delta(x - r_+)\,, \quad \ell < x < L\,; \qquad g_{1x} = 0 \quad \text{at} \quad x = \ell\,, L\,.$$

The inhibitor field $h(x)$ and the spike height $H_+ = h(r_+)$ are given by

$$\text{(A.3)} \qquad h(x) = 6H_+^2\mu_+^{3/2} g_1(x, r_+)\,, \qquad H_+ = \frac{\mu_+^{-3/2}}{6g_1|_{x=r_+}}\,,$$

where $\mu_+ \equiv \mu(r_+)$. Similarly, for the left interval $-L < x < \ell$ with a spike at $x = -r_-$, we obtain that r_- satisfies

$$\text{(A.4)} \qquad -\frac{\mu'(-r_-)}{\mu(-r_-)} - \frac{4}{5}\frac{\langle g_{2x}\rangle|_{x=-r_-}}{g_2|_{x=-r_-}} = 0\,,$$

where $g_2(x, r_-)$ satisfies

$$\text{(A.5)} \qquad g_{2xx} - g_2 = -\delta(x + r_-)\,, \quad -L < x < \ell\,; \qquad g_{2x} = 0 \quad \text{at} \quad x = \ell\,, -L\,.$$

The inhibitor field $h(x)$ and the spike height $H_- = h(-r_-)$ are given by

$$\text{(A.6)} \qquad h(x) = 6H_-^2\mu_-^{3/2} g_2(x, r_-)\,, \qquad H_- = \frac{\mu_-^{-3/2}}{6g_2|_{x=-r_-}}\,,$$

where $\mu_- = \mu(-r_-)$.

Since $\mu(x)$ is even, we have $\mu(-r_-) = \mu(r_-)$ and $\mu'(-r_-) = -\mu'(r_-)$. Next, we set $\tilde{x} = -x$ in (A.5) and label $\tilde{g}_2(\tilde{x}, r_-) \equiv g_2(-\tilde{x}, r_-)$, so that (A.4) becomes

$$\text{(A.7)} \qquad -\frac{\mu'(r_-)}{\mu(r_-)} - \frac{4}{5}\frac{\langle \tilde{g}_{2\tilde{x}}\rangle|_{\tilde{x}=r_-}}{g_2|_{\tilde{x}=r_-}} = 0\,,$$

where $\tilde{g}_2(\tilde{x}, r_-)$ satisfies

$$\text{(A.8)} \qquad \tilde{g}_{2\tilde{x}\tilde{x}} - \tilde{g}_2 = -\delta(\tilde{x} - r_-)\,, \quad -\ell < \tilde{x} < L\,; \qquad g_{2\tilde{x}} = 0 \quad \text{at} \quad \tilde{x} = -\ell\,, L\,.$$

To combine (A.1) and (A.7) into a unified expression it is convenient to define $g(x, r; \ell)$ as in (3.11), so that $g_1(x, r_+) = g(x, r_+; \ell)$ and $\tilde{g}_2(x, r_-) = g(x, r_-; -\ell)$. In this way, (A.1) and (A.7) reduce to $f(r_+,\ell)=0$ and $f(r_-,-\ell)=0$, where $f(r,\ell)$ is defined in (3.10b). The condition that the inhibitor field is continuous across $x=\ell$, as obtained by equating the two expressions for $h(\ell)$ in (A.3) and (A.6), yields the continuity condition $\xi(r_+,\ell)=\xi(r_-,-\ell)$ as written in (3.10b).

The computation of two-spike equilibria reduces to finding roots of $\boldsymbol{F}(\mathbf{u},\zeta)=0$, as defined in (3.18) as the parameter vector $\zeta\equiv(b,L)^T$ is varied. To compute paths of solutions we employ the software packages AUTO (cf. [7]) and COCO (cf. [3]) and provide the Jacobian matrices

$$D_u\boldsymbol{F}=\begin{pmatrix} \frac{\partial f}{\partial r}(r_+,\ell) & 0 & \frac{\partial f}{\partial l}(r_+,\ell) \\ 0 & \frac{\partial f}{\partial r}(r_-,-\ell) & -\frac{\partial f}{\partial \ell}(r_-,\ell) \\ \frac{\partial \xi}{\partial r}(r_+,\ell) & -\frac{\partial \xi}{\partial r}(r_-,-\ell) & \frac{\partial \xi}{\partial l}(r_+,\ell)+\frac{\partial \xi}{\partial l}(r_-,-\ell) \end{pmatrix}, \tag{A.9}$$

$$D_\zeta\boldsymbol{F}=\begin{pmatrix} \frac{\partial f}{\partial b}(r_+,\ell) & \frac{\partial f}{\partial L}(r_+,\ell) \\ \frac{\partial f}{\partial b}(r_-,-\ell) & \frac{\partial f}{\partial L}(r_-,-\ell) \\ \frac{\partial \xi}{\partial b}(r_+,\ell)-\frac{\partial \xi}{\partial b}(r_-,-\ell) & \frac{\partial \xi}{\partial b}(r_+,\ell)-\frac{\partial \xi}{\partial L}(r_-,-\ell) \end{pmatrix}. \tag{A.10}$$

By using (3.16) for f and ξ, we can calculate the entries in the Jacobians analytically as

$$\begin{aligned}
\frac{\partial f}{\partial r} &= \left[\frac{4\cosh(2r-\ell-L)-2(\tanh(r-\ell)+\tanh(r-L))\sinh(2r-\ell-L)}{5\cosh(r-L)\cosh(r-\ell)}\right] \\
&\qquad\qquad + \frac{2b(1-br^2)}{(1+br^2)^2}\,, \\
\frac{\partial f}{\partial \ell} &= \frac{2}{5}\left[\frac{\sinh(2r-\ell-L)\tanh(r-\ell)-\cosh(2r-\ell-L)}{\cosh(r-L)\cosh(r-\ell)}\right], \\
\frac{\partial f}{\partial b} &= \frac{2r}{(1+br^2)^2}\,, \\
\frac{\partial f}{\partial L} &= \frac{2}{5}\left[\frac{\sinh(2r-\ell-L)\tanh(r-L)-\cosh(2r-\ell-L)}{\cosh(r-L)\cosh(r-\ell)}\right], \\
\frac{\partial \xi}{\partial r} &= \frac{\sinh(\ell-L)}{6(1+br^2)^{5/2}}\left[\frac{3br+(1+br^2)(2\tanh(r-\ell)+\tanh(r-L))}{\cosh^2(r-\ell)\cosh(r-L)}\right], \\
\frac{\partial \xi}{\partial \ell} &= \frac{(1+br^2)^{-3/2}}{6}\left[\frac{2\tanh(r-\ell)\sinh(L-\ell)-\cosh(L-l)}{\cosh^2(r-\ell)\cosh(r-L)}\right], \\
\frac{\partial \xi}{\partial b} &= -\frac{r^2(1+br^2)^{-5/2}}{4}\left[\frac{\sinh(L-\ell)}{\cosh^2(r-\ell)\cosh(r-L)}\right], \\
\frac{\partial \xi}{\partial L} &= \frac{(1+br^2)^{-3/2}}{6}\left[\frac{\cosh(L-\ell)+\sinh(L-\ell)\tanh(r-L)}{\cosh^2(r-\ell)\cosh(r-L)}\right].
\end{aligned} \tag{A.11}$$

Finally, in Fig. 14 we include the Maple code used to compute the symmetry-breaking bifurcation point as well as parameter set where this bifurcation switches from subcritical to supercritical. This was described in (3.20) and (3.21) of §3.3.

REFERENCES

[1] V. Brena-Medina, A. Champneys, C. Grierson, M. J. Ward, *Mathematical modeling of plant root hair initiation: dynamics of localized patches*, SIAM J. Appl. Dyn. Sys., **13**(1), (2014), pp. 210–248.

```
> restart;
> rp := -fl/fr:
  Wp := xir*rp+xil:

> f := 2*b*r/(1+b*r^2)+2*sinh(2*r-L-l)/5/cosh(r-l)/cosh(r-L);
```
$$f := \frac{2\,b\,r}{b\,r^2+1} - \frac{2\sinh(-2\,r+L+l)}{5\cosh(-r+l)\cosh(-r+L)}$$
```
> xi := (1+b*r^2)^(-3/2)*sinh(L-l)/6/cosh(r-l)^2/cosh(r-L);
```
$$\xi := \frac{\sinh(L-l)}{6\left(b\,r^2+1\right)^{3/2}\cosh(-r+l)^2\cosh(-r+L)}$$
```
> fr := diff(f,r):
  fl := diff(f,l):
  xir := diff(xi,r):
  xil := diff(xi,l):

> l:=0;
```
$$l := 0$$
```
> L:=2;
  sol:=fsolve([f,Wp], {r=0.81, b=0.05});
```
$$L := 2$$
$$sol := \{b=0.03406382360,\ r=0.8355850293\}$$
```
> L:=3;
  sol:=fsolve([f,Wp], {r=0.81, b=0.05});
```
$$L := 3$$
$$sol := \{b=0.08650427219,\ r=0.7835180270\}$$

```
> restart;
  rp := -fl/fr:
  rpp := -(frr*rp^2+2*frl*rp+fll)/fr:
  rppp := -(frrr*rp^3+3*frrl*rp^2+3*frll*rp+3*frr*rp*rpp+3*frl*rpp+
  flll)/fr:

  Wp := xir*rp+xil:
  Wppp := xirrr*rp^3+3*xirrl*rp^2+3*xirll*rp+3*xirr*rp*rpp+3*xirl*
  rpp+xir*rppp+xilll:

> f := 2*b*r/(1+b*r^2)+2*sinh(2*r-L-l)/5/cosh(r-l)/cosh(r-L);
```
$$f := \frac{2\,b\,r}{b\,r^2+1} - \frac{2\sinh(-2\,r+L+l)}{5\cosh(-r+l)\cosh(-r+L)}$$
```
> xi := (1+b*r^2)^(-3/2)*sinh(L-l)/6/cosh(r-l)^2/cosh(r-L);
```
$$\xi := \frac{\sinh(L-l)}{6\left(b\,r^2+1\right)^{3/2}\cosh(-r+l)^2\cosh(-r+L)}$$
```
> fr := diff(f,r): fl := diff(f,l): frr := diff(f,r,r):
  frl := diff(f,r,l): fll := diff(f,l,l): frrr := diff(f,r,r,r):
  frrl := diff(f,r,r,l): frll := diff(f,r,l,l): flll := diff(f,l,l,
  l):

  xir := diff(xi,r): xil := diff(xi,l): xirr := diff(xi,r,r):
  xirl := diff(xi,r,l): xill := diff(xi,l,l): xirrr := diff(xi,r,r,
  r):
  xirrl := diff(xi,r,r,l): xirll := diff(xi,r,l,l): xilll := diff
  (xi,l,l,l):

> l:=0;
  sol:=fsolve([f, Wp, Wppp], {r=0.8, L=2.1, b=0.08});
```
$$l := 0$$
$$sol := \{L=2.597190816,\ b=0.07596727744,\ r=0.7926550122\}$$

Fig. 14: Maple code to compute the bifurcation point (left panel) from (3.20) and the second-order bifurcation point (right panel) from (3.21), which corresponds to the switch between a subcritical and a supercritical symmetry-breaking bifurcation.

[2] C. N. Chen, S. I. Ei, S. Tzeng, *Heterogeneity-induced effects for pulse dynamics in Fitzhugh-Nagumo-type systems*, Physica D, **382-383**(1), (2018), pp. 22–32.

[3] H. Dankowicz, F. Schlider, *Recipes for continuation*, in the book series *Computational Sciences and Engineering*, SIAM Publications, (2013), xv + 564 pages.

[4] A. Doelman, R. A. Gardner, T. Kaper, *Large stable pulse solutions in reaction-diffusion equations*, Indiana U. Math. J., **50**(1), (2001), pp. 443-507.

[5] A. Doelman, T. Kaper, *Semistrong pulse interactions in a class of coupled reaction-diffusion equations*, SIAM J. Appl. Dyn. Sys., **2**(1), (2003), pp. 53-96.

[6] A. Doelman, T. Kaper, K. Promislow, *Nonlinear asymptotic stability of the semi-strong pulse dynamics in a regularized Gierer-Meinhardt model*, SIAM J. Math. Anal., **38**(6), (2007), pp. 1760–1789.

[7] E. J. Doedel, A. R. Champneys, T. Fairgrieve, Y. Kuznetsov, B. Oldeman, R. Paffenroth, B. Sandstede, X. Wang, C. Zhang, *Auto07p: Continuation and bifurcation software for ordinary differential equations*, Technical report, Concordia University, 2007.

[8] A. Gierer, H. Meinhardt, *A theory of biological pattern formation*, Kybernetik, **12**, (1972), pp. 30–39.

[9] L. Harrison, D. Holloway, *Order and localization in reaction-diffusion pattern*, Physica A, **222**, (1995), pp. 210-233.

[10] P. van Heijster, C. N. Chen, Y. Nishiura, T. Teramoto, *Pinned solutions in a heterogeneous three-component Fitzhugh-Nagumo model*, J. Dyn. Diff. Eq., **31**(1), (2019), pp. 153–203.

[11] D. Holloway, L. Harrison, J. Armstrong, *Computations of post-inductive dynamics in axolotl heart formation*, Developmental Dynamics, **200**, (1994), pp. 242-256.

[12] D. Holloway, *Reaction-diffusion theory of localized structures with applications to vertebrate organogenesis*, Ph. D. thesis in Chemistry, University of British Columbia, (1995).

[13] A. Hunding, *Bifurcations in Turing systems of the second kind may explain blastula cleavage plane orientation*, J. Math. Biol., **25**(2), (1987), pp. 109-121.

[14] D. Iron, M. J. Ward, J. Wei, *The stability of spike solutions to the one-dimensional Gierer-Meinhardt model*, Physica D, **150**(1-2), (2001), pp. 25–62.

[15] D. Iron, M. J. Ward, *The dynamics of multi-spike solutions to the one-dimensional Gierer-Meinhardt model*, SIAM J. Appl. Math., **62**(6), (2002), pp. 1924-1951.

[16] T. Kolokolnikov, S. Xie, *Spike density distribution for the Gierer-Meinhardt model with precursor*, Physica D, **31**, 132247, (2019)

[17] T. Kolokolnikov, J. Wei, *Hexagonal spike clusters for some PDE's in 2-D*, to appear, DCDS-B, (2020).

[18] T. Kolokolnikov, J. Wei, *Pattern formation in a reaction-diffusion system with space-dependent feed rate*, SIAM Review, **60**(3), (2018), pp. 626–645.

[19] A. Krause, V. Klika, T. E. Woolley, E. A. Gaffney, *Heterogeneity induces spatiotemporal oscil-*

lations in reaction-diffusion systems, Phys. Rev. E **97**(5), 052206, (2018).
[20] A. Krause, V. Klika, T. E. Woolley, E. A. Gaffney, *From one pattern into another: Analysis of Turing patterns in heterogeneous domains via WKBJ*, preprint, arXiv:1908.07219 [nlin.PS].
[21] H. Meinhardt, *Models of Biological Pattern Formation*, Academic Press, London (1982).
[22] K. Page, P. K. Maini, N. A. M. Monk, *Pattern formation in spatially heterogeneous Turing reaction-diffusion models*, Physica D, **181**(1-2), (2003), pp. 80–101.
[23] K. Page, P. K. Maini, N. A. M. Monk, *Complex pattern formation in reaction-diffusion systems with spatially varying parameters*, Physica D, **202**(1-2), (2005), pp. 95–115.
[24] W. Sun, M. J. Ward, R. Russell, *The slow dynamics of two-spike solutions for the Gray-Scott and Gierer-Meinhardt systems: competition and oscillatory instabilities*, SIAM J. App. Dyn. Sys., **4**(4), (2005), pp. 904–953.
[25] J. C. Tzou, A. Bayliss, B. J. Matkowsky, V. A. Volpert, *Stationary and slowly moving localized pulses in a singularly perturbed Brusselator model*, Europ. J. Appl. Math., **22**(5), (2011), pp. 423–453.
[26] J. C. Tzou, Y. Nec, M. J. Ward, *The stability of localized spikes for the 1-d brusselator reaction-diffusion model*, Europ. J. Appl. Math., **24**(4), (2013), pp. 515–564.
[27] M. J. Ward, D. McInerney, P. Houston, D. Gavaghan, P. Maini, *The dynamics and pinning of a spike for a reaction-diffusion model*, SIAM J. Appl. Math., **62**(4), (2002), pp. 1297–1328.
[28] M. J. Ward, J. Wei, *Hopf bifurcations and oscillatory instabilities of spike solutions for the one-dimensional Gierer-Meinhardt model*, J. Nonlinear Science, **13**(2), (2003), pp. 209-264.
[29] M. J. Ward, J. Wei, *Asymmetric spike patterns for the one-dimensional gierer-meinhardt model: equilibria and stability*, Europ. J. Appl. Math., **13**(3), (2002), pp. 283–320.
[30] J. Wei, *Existence and stability of spikes for the Gierer-Meinhardt system*, book chapter in *Handbook of Differential Equations, Stationary Partial Differential Equations*, Vol. 5 (M. Chipot ed.), Elsevier, (2008), pp. 489–581.
[31] M. Winter, J. Wei, *On the Gierer-Meihhardt system with precursors*, DCDS-A, **25**(1), (2009), pp. 363–398.
[32] J. Wei, M. Winter, *Stable spike clusters for the one-dimensional Gierer-Meinhardt system*, Europ. J. Appl. Math, **28**(4), (2017), pp. 576–635.